BNL 50479

HTGR SAFETY EVALUATION DIVISION

QUARTERLY REPORT
July 1 - September 30, 1975

DEPARTMENT OF APPLIED SCIENCE

BROOKHAVEN NATIONAL LABORATORY
ASSOCIATED UNIVERSITIES, INC.
UNDER CONTRACT NO. E(30-1)-16 WITH THE
UNITED STATES ENERGY RESEARCH AND DEVELOPMENT ADMINISTRATION

BNL 50479
(Advanced Reactor Safety Research,
Gas-Cooled Reactors - NRC-8)

HTGR SAFETY EVALUATION DIVISION

QUARTERLY REPORT
July 1 - September 30, 1975

DONALD G. SCHWEITZER, Head
HTGR Safety Evaluation Division

The High Temperature Gas Cooled Reactor (HTGR) Safety Evaluation Division provides research and analytical support to the Nuclear Regulatory Commission (NRC), Office of Nuclear Regulatory Research (RSR), on all aspects of HTGR's regarding public safety. In addition to BNL personnel, the HTGR Safety Evaluation Division uses a wide national and international base of consulting expertise for RSR by close collaboration with consultants and subcontractors at universities and scientific establishments.

This work was performed under the auspices of the Nuclear Regulatory Commission Contract No. E(30-1)-16.

BROOKHAVEN NATIONAL LABORATORY
UPTON, NEW YORK 11973

NOTICE

Printed in the United States of America
Available from
National Technical Information Service
U.S. Department of Commerce
5285 Port Royal Road
Springfield, VA 22161
Price: Domestic $7.00; Foreign $9.50;
Microfiche $2.25

January 1976 375 copies

TABLE OF CONTENTS

Summary

Construction of the apparatus for measuring metal fission product adsorption isotherms on H451 graphite has been completed. Preliminary experiments measuring the vapor pressure of elemental cesium by the Knudsen effusion technique have been started. A review of available vapor pressure data for cesium has been completed.

The requirements of an in-pile loop experiment to estimate maximum hypothetical fission product release have been evaluated. A preirradiated HTGR fuel element fully irradiated and stepwise heated in the region 1400°C to 2100°C is required for an experiment to understand the influence of fuel particle coating failure.

A program has been initiated to study fuel kernel oxidation/hydrolysis. The initial phase will consist of an investigation of the fuel kernel reaction with CO. A second phase of the program will involve studying the influence of H_2O. A thermochemical data evaluation is now in progress to evaluate the influence of oxidizing impurity gases (H_2O and O_2) in helium on fission products. An interesting conclusion is that if equilibrium thermodynamics is assumed to be relevant when hydroxide formation is considered, strontium partial pressure in the vapor phase (as $Sr(OH)_2$) will be increased by two orders of magnitude for an H_2O level of 100 ppm in helium at 1000°K.

Oxygen activity meters were used to demonstrate their applicability to monitor impurities in helium and to study reaction rates. Fair agreement was obtained between observed potentials and those

calculated from known oxygen concentrations. Results from monitoring reaction rates of gaseous impurities with iron-impregnated graphite were obtained as a function of gas flow rate. The rates appear highly complex and require further study. A detailed series of resistance measurements were conducted as a function of temperature on a ZrO_2-Y_2O_3 cell to be used in the helium impurities loop. This data will be used to characterize changes in the cell as a function of time.

The Helium Impurities Loop has been assembled and successfully operated at the design conditions of 1400°F and 5.8 lb/h. Graphite and metallic test specimens are being prepared for the first test run of the loop. Preliminary chromatograms obtained using a gas chromatograph with a thermal conductivity detector indicate the instrument will be able to resolve and detect H_2, O_2, N_2, CH_4, and CO.

Large sections (logs) of PGX and ATJ graphite were received and sectioned into samples for chemical analysis and other studies. The ATJ graphite samples will be the first to be analyzed. The method will consist of employing an emission spectroscope to analyze ground and powdered samples of the graphite.

The core seismic studies for the horizontal array model have shown that the dynamic response of the 30 mass model can be accurately predicted with a reduced mass system. The studies show that both the frequency of maximum response and the maximum force transmitted to the PCRV are the same for the 5, 7, 9 and 30 mass models. This con-

clusion prevails under the worst conditions where the forces generated are maximum.

The dynamic analysis of a block model of the core structure has shown that a sub-harmonic response could easily be revealed for harmonic excitation of the core. To investigate this a forcing function composed of two sine waves was imposed on a non-linear system with cubic elasticity. The results of this investigation were remarkably different from those that were obtained with the forcing functions taken separately. This holds even if the primary coefficient is quite small but still greater than a minimum threshold level.

The development of a vertical array code is near completion. Using this code an evaluation of the characteristics of a single rocking block was undertaken. The response for this system showed a softening-hardening spring characteristic. That is, at certain frequencies within the non-linear range, three stable solutions could be obtained. For simple sinusoidal sweep runs, either up or down, only the lower two stable roots are evident. However, with the proper initial conditions and a sinusoidal sweep run, the highest branch is apparent.

The response of the cover plate of the thermal insulation of the PCRV (prestressed concrete reactor vessel) of the HTGR (High Temperature Gas Cooled Reactor) excited by the turbulent flow noise depends on the natural resonance frequencies and displacement modes of that plate. An experimental program is described herewith which

determined those resonance frequencies and modes. The case of a flat plate clamped in the middle of its four sides and also when one of the four bolts has failed, has been considered in this work. Thirty-three resonances in the range 30.5 to 736 Hz have been identified for the four bolts normal operation and forty-two in the range 12.5 to 496.1 Hz for the three bolts accidental situation. Of particular interest to the turbulent flow noise response, the modes symmetrical to the X-Y and diagonal axis have been identified and classified in a two dimensional matrix form for the mn + nm and mn - nm modes combination (m and n being the pure modes along the X-Y axis respectively.

Equipment for elevated temperature and room temperature mechanical testing of metallic and graphitic HTGR materials is being investigated for purchase. The equipment being evaluated includes low-cycle-fatigue, creep-fatigue, stress-rupture and tensile-test machines. High-cycle-fatigue tests with zero mean loads have continued for Incoloy 800 at 1100° and 1400°F. The 1400°F data indicate that if an endurance limit exists, it will be very low. An effort to collect material property data has been started. The effort has thus far concentrated on obtaining the more readily available data on graphites and metals.

Crack propagation studies have been conducted on ATJ and H451 graphites in the electron microscope using the wedge-opening technique. Equipment for oxidation studies of graphite has been set up to determine the effects of oxidation on the crack propagation in

graphites. An analytical model which computes the tensile and compressive fracture strengths has been used to predict the properties of the graphite. The results obtained with this model closely predict the observed properties of the graphite. Increasing the pore volume of ATJ graphite leads to a decrease in both compressive and tensile strengths. A 10% increase in pore volume gave about a 10% decrease in mechanical properties.

A parametric sensitivity analysis was done using the graphite oxidation program GOPTWO. By studying the effects of varying the graphite-water reaction rates, the diffusion coefficient of steam in graphite, and the water ingress rate, an appreciation of which physical entities in an HTGR system are important was obtained. Furthermore, the results of the computations were compared to corresponding results obtained previously with the OXIDE-3 code. Good agreement between the two codes was observed over the entire range of variables studied.

The equilibrium full power study of the graphite oxidation due to a fixed steam leak has been extended. In the previous quarter, information was obtained about the sensitivity of the results to variation in leak rate and reaction rate. The present study is supplementary in that the sensitivity of the results to a variation of the porosity-tortuosity factor in the gas-graphite diffusion constant is investigated. All three parameter variations have been analyzed and fuel hydrolysis under operating conditions is discussed based on the analytical results.

PAGE TORN →

The steam tube rupture accident with scram that is discussed in Section 9 of GA-LTR-7 is herein extended to 200 ksec in time and evidence of incorrect programming of the fuel hydrolysis is implied by the results.

Preliminary results are described dealing with circumstances under which combustion phenomena may occur following depressurization accidents. Discussions are included relating to the consequences, physical characteristics and potential destructive power of the combustion phenomena.

I. Fission Product Release and Transport

A. Adsorption of Metallic Fission Products (S. Aronson, R. Behrens -- Brooklyn College)

Experimental

Construction of the apparatus for measuring metal fission product adsorption isotherms on H451 graphite has been completed. Preliminary experiments measuring the vapor pressure of elemental cesium by the Knudsen effusion technique have been started.

The following modifications on the vaporization apparatus have been made:

1. The Knudsen cell and thermocouple support arrangement has been modified. Three rods of 304 stainless steel attached to a flange at the end of the quartz vaporization tube extend the length of the tube to the furnace region. The crucible rests on and is held tightly in place by the rods.

2. The thermocouple for measuring the effusion cell temperature now comes into the vacuum system through a feedthrough on the flange holding the support rods. The crucible support and the thermocouple can be removed as a complete unit by simply unbolting the flange.

3. The Pt-Pt, 13% Rh thermocouple to be used for measuring the effusion cell temperature in the sorption experiments has been temporarily replaced by a chromel-alumel (Type K) thermocouple to be used in the elemental cesium vapor pressure experiments.

The high temperature furnace is found to have a 1 1/2 to

2 inch zone in which the temperature is constant to $\pm 1^{\circ}C$. The furnace is positioned around the vaporization tube such that the effusion cell and the thermocouple are within this constant temperature zone. Control of the effusion cell temperature was found to be satisfactory. At $850^{\circ}C$ control to $\pm 0.5^{\circ}C$ is easily achieved while at lower temperature control of $\pm 0.1^{\circ}C$ for one to three hours and $\pm 0.25^{\circ}C$ for longer periods of time can be routinely achieved. To be sure that the thermocouple, situated 1-2 mm from the crucible bottom, correctly measures the crucible temperature, a chromel-alumel thermocouple, previously calibrated against the melting point of tin, was placed directly inside a molybdenum effusion cell and its emf measured simultaneously with that of the permanent thermocouple.

A 336.6 mg sample of 99.98% pure elemental cesium tagged with 0.1 mCi of cesium-134 has been placed in a clean, outgassed molybdenum effusion cell and put into place within the vaporization apparatus. Handling of the cesium is conducted under an argon atmosphere inside a dry box. A small plug of paraffin wax is placed in the effusion cell orifice so as to seal the cesium from air during transfer of the cell from the dry box to the vaporization apparatus.

The NaI scintillation detector housed in a lead pig on an X-Y-Z table "sees" the effusion cell through a 3/4 inch diameter hole in the lead shielding. The detector is positioned as close to the crucible as the furnace will allow (about 10 inches). The height of the detector and its position along the length of the vaporization

tube are then adjusted to yield a maximum count rate. Count rates are determined by counting the full gamma spectrum of ^{134}Cs with the spectroscopy amplifier gain set approximately midway between the maximum and minimum settings and with the single channel analyzer baseline set to eliminate counts due to low amplitude noise. The photomultiplier voltage is set at 1125 volts. An initial count rate is determined prior to heating the sample. The background count rate is also checked prior to insertion of the cesium sample into the vaporization tube.

The rate of mass loss from the crucible through the orifice of area $\underline{a}$ (cm^2) at a particular temperature $\underline{T}$ (^oK) is computed from the fraction of cesium remaining in the effusion cell at times $\underline{t}_1$ and $\underline{t}_2$ as determined by the respective count rates $\underline{R}_{t_1}$ and $\underline{R}_{t_2}$ and the initial count rate determined at the beginning of the experiment, $\underline{R}_i$. The fraction of cesium remaining in the cell at time $\underline{t}$ is R_t/R_i. The rate of effusion (mg/min) of vapor over the time interval $t_2 - t_1$ is:

$$\frac{(336.6)(R_{t_1} - R_{t_2})}{(t_2 - t_1)\, R_i}$$

The vapor pressure of cesium is then computed from the measured effusion rate using the Hertz-Knudsen-Langmuir equation:

$$P(atm) = 3.7596 \times 10^{-7}\ (R/W_a a)(T/M)^{1/2}$$

where

$\underline{R}$ = rate of weight loss (mg/min) from cell with orifice area $\underline{a}$ cm^2

$\underline{P}$ = vapor pressure in atmospheres

$\underline{M}$ = molecular weight of effusing vapor

$\underline{W}_a$ = orifice Clausing factor

As of the end of the current report period six data points have been taken between 70°C and 190°C. Effusion rates are found to be about a factor of ten too high. This has been found to be caused by cesium vapor leaking from the connection between the effusion cell lid and bottom.

Thermochemical Data Evaluation

A review of available literature vapor pressure data[1-1 to 1-22] for cesium has been completed. The results are presented in Table 1-1. Values of $\Delta H^o(T)$ and $\Delta S^o(T)$ for the reaction Cs(l) = Cs(g) have been recomputed for each set of literature data. The results are given in columns 6 and 7 of Table 1-1. Second-law and third-law values of the enthalpy change for the above reaction have also been computed and are listed in columns 8 and 9, respectively. The calculations were performed using a FORTRAN program called DELH, a brief description of which is given in an informal BNL report.

Vapor pressures above 500°K were corrected for the presence of cesium dimer using a value of $\Delta H^o(298)$ = 10.71 kcal for the dissociation energy[1-23] of $Cs_2(g)$ and free energy functions for Cs(g) and $Cs_2(g)$ given by JANAF[1-24]. Free energy functions for Cs(l) used in

Table 1-1

Review of Literature Data on the Vapor Pressure of Liquid Cesium - Cs(l) = Cs(g)

Authors (Reference)	Method	Temp. Range (°K)	No. of Data Points	T_{avg} (°K)	$\Delta H^{o}(T)$ (kcal $mole^{-1}$)	$\Delta S^{o}(T)$ (cal K^{-1} $mole^{-1}$)	$\Delta H^{o}(II,298)$ (kcal $mole^{-1}$)	$\Delta H^{o}(III,298)$ (kcal $mole^{-1}$)
Pradel, Roussel, Spiess[1-1]	Optical	306-312	5	308	14.00±1.81	7.37±5.86	(14.48±1.81)	18.39±0.04
Taylor, Langmuir[1-2]	Thermionic Emission	303-346	6	322	17.70±0.10	19.47±0.32	18.23±0.10	18.35±0.01
Buck, Pauly[1-3]	Optical	319-348	2	333	17.58	19.07	18.14	18.37±0.01
Scott[1-4]	Static	321-387	8	352	16.85±0.28	19.29±0.79	(17.47±0.27)	(17.57±0.04)
Fuchtbauer, Bartels[1-5]	Static	464-506	4	479	16.86±0.80	17.12±1.68	(17.87±0.79)	18.00±0.05
Kroner[1-6]	Static	523-629	12	575	18.13±0.46	19.55±0.81	(19.30±0.45)	18.61±0.09
Hackspill[1-7]	Static	503-670	10	587	17.12±0.82	17.88±1.41	18.28±0.80	18.57±0.23
Volyak, Vinogradov Anisimov[1-8]	Static	564-947	44	809	17.36±0.09	18.34±0.11	18.86±0.07	18.45±0.08
Achener[1-9]	Static	752-1144	15	925	16.63±0.03	17.44±0.03	18.46±0.04	18.45±0.02
Ruff, Johannsen[1-10]	Boiling Point	-	1	943	-	-	-	18.15
Shipl'rain, et al.[1-11]	Static	785-1085	-	935	15.97	16.78	(17.82)	18.40
Bodhansky, Schins[1-12]	Static	723-1137	17	948	16.68±0.07	17.60±0.07	18.53±0.07	18.35±0.05
Tepper, Murchison, Zelenak, Roehlich[1-13]	Boiling Point	729-1268	21	953	16.50±0.03	17.32±0.03	18.44±0.02	18.42±0.02

Table 1-1 Cont'd.

Authors (Reference)	Method	Temp. Range (°K)	No. of Data Points	T_{avg} (°K)	$\Delta H^{o}(T)$ (kcal mole^{-1})	$\Delta S^{o}(T)$ (cal K^{-1} mole^{-1})	ΔH^{o}(II,298) (kcal mole^{-1})	ΔH^{o}(III,298) (kcal mole^{-1})
Schins, van Wijk, Dorpema[1-14]	Boiling Point	723-1139	59	974	16.75±0.04	17.65±0.04	18.61±0.04	18.37±0.05
Bonilla, Sawheny, Mekansi[1-15]	Static	674-1199	41	1020	16.58±0.03	17.48±0.03	18.47±0.02	18.33±0.04
Shipl'rain, Belova[1-16]	Static	823-1198	121	1030	16.27±0.02	17.13±0.02	18.33±0.01	18.40±0.01
Young[1-17]	Static	811-1255	-	1033	18.55	19.01	(20.62)	18.74
Cochran[1-18]	Static	811-1255	-	1033	18.85	19.03	(20.92)	18.97
Stone, et al.[1-19]	Static	921-1287	82	1083	16.24±0.02	17.11±0.02	18.52±0.02	18.39±0.02
Cherneeva, Proskurin[1-20]	Static	1028-1293	32	1157	16.02±0.04	16.92±0.03	18.52±0.04	18.38±0.02
Ewing, et al.[1-21]	Static	1118-1221	7	1171	15.80±0.44	16.71±0.37	18.36±0.45	18.41±0.04
Stone, et al.[1-22]	Static	980-1291	33	1188	14.19±2.70	14.28±2.29	(16.64±2.70)	(19.68±1.20)
						Average	18.44±0.14	18.40±0.05

NOTE: Results in parenthesis are not included in average.

the evaluation are those previously reported by us[1-25].

All vapor pressure studies of cesium reported in the literature were performed using static techniques with the exception of the investigation by Taylor and Langmuir[1-2] who performed a Langmuir or free-vaporization experiment. The five low temperature vapor pressure studies[1-1 to 1-5] (10^{-4}-10^{-8} atm) are in poor agreement with one another. Only the results of Buck and Pauly[1-3] and Taylor and Langmuir appear to be in agreement with the high temperature data.

A Knudsen effusion check of the cesium vapor pressure in the 10^{-4} to 10^{-8} atmosphere region is presently under way in this laboratory as described above. This check is important because while the majority of the high temperature results and the two low temperature results give consistent second- and third-law values of $\Delta H^{o}(298)$, some uncertainty may be present in the third-law values due to uncertainty in the dissociation energy of $Cs_2(g)$ and in the free energy functions for Cs(l) at high temperature.

B. Fission Product Hydrolysis/Oxidation (D. Chandra, S. Aronson)

In OXIDE-3, no account has been taken of the influence of H_2O or CO on fission product transport and distribution. Following a steam or air ingress accident, volatile metallic fission products already released from the fuel and may come in contact with steam

or oxygen and form volatile hydroxides and oxides. This aspect of the problem is under investigation according to the following general guidelines: (1) initial screening of fission products from the volatility of their oxides and hydroxides, and (2) the fission products so screened, will be investigated based on existing thermodynamic and sorption data. The formation of oxides and hydroxides in the presence of C, H_2O, CO, H_2 without sorption, with sorption and with co-sorption assumed will be evaluated.

After gaining some understanding from the above, the main goal will be to establish the best possible experiment to study fission product transport under impurity ingress conditions.

An extensive literature survey has been started. The initial phase consisted of locating volatile fission product oxides in equilibrium with their respective condensed phases for a range of oxygen partial pressures and volatile fission product hydroxides in equilibrium with pure water vapor and their oxides. This was an order of magnitude evaluation to isolate the fission product elements to be subjected to a subsequent thermodynamic analysis. One major difficulty in this area is the limited availability of data on the formation of hydroxides. The fission products with volatile oxides and hydroxides were Cs, Rb, Ru, Mo, Tc and Sr.

A thermodynamic analysis has been started to estimate the hydroxide to metal vapor ratios for a certain water vapor partial pressure and temperature both with and without carbon entering the reaction. Preliminary results are given in Table 1-2. Detailed

Table 1-2

Calculated Metal Hydroxide/Metal Vapor Pressure Ratio.

Values Calculated at 1000°K and $P_{H_2O} = 5 \times 10^{-3}$ atm.

Using Data from References[1-26,1-27]

Species	Vapor Ratio: Metal hydroxide / Metal Without C	Vapor Ratio: Metal hydroxide / Metal With C
$\frac{P_{Cs(OH)}}{P_{Cs}}$	5.9×10^{4}	0.2
$\frac{P_{Sr(OH)_2}}{P_{Sr}}$	8.7×10^{12}	1.0×10^{2}
$\frac{P_{SrOH}}{P_{Sr}}$	3.4×10^{4}	0.11
$\frac{P_{MoOH}}{P_{Mo}}$	2.8×10^{5}	0.94
$\frac{P_{Mo(OH)_2}}{P_{Mo}}$	1.1×10^{15}	1.2×10^{4}
$\frac{P_{RuOH}}{P_{Ru}}$	1.6×10^{3}	5.4×10^{-3}
$\frac{P_{Ru(OH)_2}}{P_{Ru}}$	4.3×10^{5}	4.7×10^{-6}
$\frac{P_{TcOH}}{P_{Tc}}$	2.35×10^{3}	7.8×10^{-3}
$\frac{P_{Tc(OH)_2}}{P_{Tc}}$	6.7×10^{8}	7.5×10^{-3}
$\frac{P_{RbOH}}{P_{Rb}}$	9.5×10^{2}	3.2×10^{-3}

calculations to determine the influence of changing water vapor concentrations and temperature are now in progress.

Some interesting conclusions can be drawn. At $1000^{o}K$ with 5×10^{-3} atm H_2O, only Sr and Mo show considerably higher hydroxide vapor pressure compared to the metal vapor pressure. However, the vapor pressure of Mo at $1000^{o}K$ is so low that it can be ignored for all practical purposes at this temperature.

It appears from the vapor pressures that almost all the strontium will be present as hydroxides at this temperature and water vapor concentrations.

The influence of the phenomenon on the sorption isotherm of Sr in graphite is now being analyzed.

Additional investigations are in progress in the following areas:

(1) The influence of sorption on other fission products. The elements being studied are Cs, Rb.

(2) The influence of oxygen.

(3) The importance of the formation of transition metal carbonyls.

References

1-1 P. Pradel, F. Roussel and G. Spiess, Rev. Sci. Instrum. 45, 45 (1974).

1-2 J. Taylor and I. Langmuir, Phys. Rev. 51, 423 (1937).

1-3 U. Buck and H. Pauly, Z. Phys. Chemie, N. F. 44, 345 (1965).

1-4 D. Scott, Phil. Mag. 47, 32 (1924).

1-5 C. Fuchtbauer and H. Bartels, Z. Physik 4, 337 (1921).

1-6 A. Kroner, Ann. Physik. 40, A438 (1913).

1-7 M. L. Hackspill, Ann. Chim. et Phys. 28, 613 (1913).

1-8 L. D. Volyak, Y. K. Vinogradov and V. M. Anisimov, High Temp. 6, 521 (1968).

1-9 P. Y. Achener, AGN-8090 (1964); ORNL-3605, Vol. 1, p. 3 (1964).

1-10 O. Ruff and O. Johannsen, Berichte 38, 360 (1905).

1-11 E. E. Shipl'rain, Y. A. Soldatenko, K. A. Yakimovich, V. A. Fomin, V. A. Savchanko, A. M. Belovo, D. N. Kagan and I. F. Krainova, High Temp. 3, 870 (1965).

1-12 J. Bodhansky and H. E. J. Schins, J. Phys. Chem. 71, 215 (1967); J. Appl. Phys. 36, 3683 (1965).

1-13 F. Tepper, A. Murchison, J. Zelenak and F. Roehlich, MSAR-63-56 (1963); ORNL-3605, Vol. 1, p. 26 (1964).

1-14 H. E. J. Schins, R. W. M. van Wijk and B, Dorpema, Z. Metallkde 62, 330 (1971).

1-15 C. F. Bonilla, D. L. Sawheny and M. M. Mekansi, Trans. ASME 55, 877 (1962).

References Cont'd.

1-16 E. E. Shipl'rain and A. M. Belova, High. Temp. 5, 477 (1967).

1-17 P. F. Young, AGN-8041 (1962).

1-18 D. L. Cochran, BNL-756(C-35) (1962).

1-19 J. P. Stone, C. T. Ewing, J. R. Spann, R. W. Steinkuller, D. D. Williams and R. R. Miller, J. Chem. Eng. Data 11, 315 (1966); NRL Report 6246 (1965).

1-20 L. I. Cherneeva and V. N. Proskurin, High Temp. 10, 687 (1972).

1-21 C. T. Ewing, J. R. Spann, J. P. Stone, E. W. Steinkuller and R. R. Miller, J. Chem. Eng. Data 15, 508 (1970).

1-22 J. P. Stone, C. T. Ewing, J. R. Spann, E. W. Steinkuller, D. D. Williams and R. R. Miller, J. Chem. Eng. Data 11, 309 (1966).

1-23 G. Herzberg, Spectra of Diatomic Molecules, D. Van Nostrand Co., Inc. (1966).

1-24 JANAF Thermochemical Tables, Second Ed., D. R. Stull and H. Prophet, Editors, NSRDS-NBS-37 (1971).

1-25 R. G. Behrens and S. Aronson, HTGR Safety Evaluation Division, Brookhaven National Laboratory, Quarterly Report, January-March 1975, BNL-50450.

1-26 R. G. Bedford and D. D. Jackson, "Volatilities of the Fission Product and Uranium Oxides," UCRL-12314.

1-27 D. D. Jackson, "Thermodynamics of Gaseous Hydroxides," UCRL-51137.

II. Primary Coolant Impurities

A. Helium Impurities Loop (A. Romano)

The detailed design and operating conditions of the Helium Impurities Loop (HIL) have been given earlier[2-1]. Room temperature operations for shake down of equipment have been concluded and resultant minor modifications to HIL have been completed. The loop was subsequently operated at the design operating conditions without difficulty. During this time, the loop was operated without specimens in the test section and without gas monitoring capability. Several additional modifications are planned.

The first HIL test section will consist of specimens of the following materials:

Material	Type of Specimen	Size
H451	Tensile	1/4" diam. x 3" long
		1/2" diam. x 3" long
ATJ	Tensile	1/4" diam. x 3" long
		1/2" diam. x 3" long
PGX	Tensile	1/2" diam. x 3" long
Incoloy 800	Corrosion Tab	1/2" x 1" x 1/8"
304 s.s.	Corrosion Tab	1/2" x 1" x 1/8"
2¼Cr 1Mo	Corrosion Tab	1/2" x 1" x 1/8"

The graphite specimens will be placed in two of the test section retorts and the metallic specimens will be located in the third retort. Typical graphite tensile specimens are shown in Figure 2-1. The specimens will be fixed to each other by means of

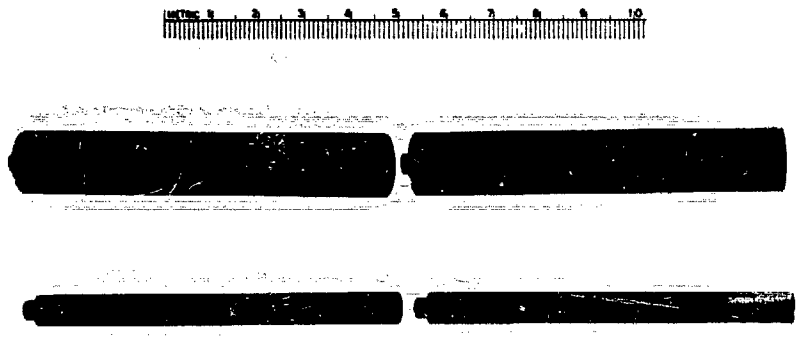

Figure 2-1. Typical graphite tensile specimens for HIL.

tight fitting joints to form columns consisting of 7 specimens in each of 8 columns. A schematic representation of the array is shown in Figure 2-2. The ATJ and PGX specimens have been completed, and the H451 and metallic specimens are presently being prepared.

Considerable difficulty has been encountered in applying the gas chromatograph (from a previous program) to the measurement of the anticipated HIL impurities. Of the three detectors and six columns available in the instrument, only two detectors and two columns are applicable. Therefore, considerable rebuilding has been required and a single, integrated gas chromatograph has now been assembled for evaluation. Preliminary chromatograms indicate the instrument can resolve and detect small concentrations (to 50 ppm) of H_2, O_2, N_2, CH_4 and CO. Modifications are required to include H_2O and CO_2 in the analysis.

B. Impurity Monitoring (H. Isaacs)

The presence of impurities in the helium coolant may lead to oxidation of graphite and alloys in the HTGR primary system at a rate depending on the impurity concentration. One factor which can lead to significant differences is the oxygen activity of the gas is the ratio of various constituents of the gas, e.g. H_2 to H_2O ratio. A rapid technique for monitoring the oxygen activity of the helium consists of a solid electrolytic cell with either thoria or zirconia doped with yttria as the oxygen electrolyte. The basic cell may be represented by

Ag,He gas $|$oxide electrolyte $|O_2$ (0.21 atmos.), Ag

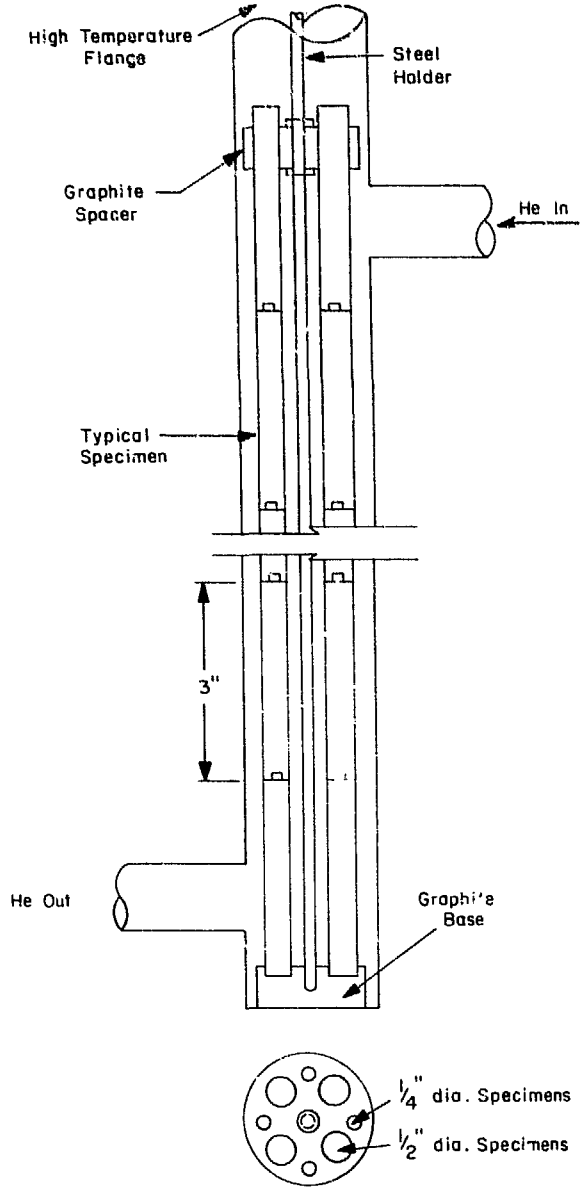

Figure 2-2. Graphite tensile specimen test section.

where the Ag is a third electronic conducting film on both the inside and outside of the tube, acting as the electrode contact. The potential of the cell is measured across the electrolyte. The right-hand side of the cell with air in contact with the silver film may be considered as a reference gas as the oxygen composition is fixed. Other reference electrode systems may be used such as a metal/metal oxide mixture which would have a fixed oxygen activity. These systems for monitoring oxygen activity respond extremely rapidly to changes in the oxygen activity and also have the possibility of being used directly in contact with the primary helium coolant.

Reaction Rate Measurements

The oxygen activity meter can be employed to study reactions of graphite with impurities. For example, a gas may be passed through an external reaction vessel on the second side of the cell. The difference in potential across the cell is a change in the oxygen potential of the system.

An experiment was conducted passing an inert carrier gas (nitrogen) with an unknown impurity into the inside of a thoria-yttria tube containing iron impregnated graphite granules approximately 3 mm in size. It was found that the potential was dependent on the flow rate. This would be expected if the oxygen containing species in gas passing through the cell did not reach equilibrium with the graphite. At high flow rates the potential approached a value almost independent of flow rate. This value was taken as the

unreacted composition of the gas. The following table lists the ratio of the composition of the gas to final value as a function of the flow rate:

Flow Rate cc/sec.	Oxygen Composition Ratio
0.21	$1.38\ 10^{-4}$
0.50	$2.69\ 10^{-3}$
0.75	$1.03\ 10^{-2}$
1.00	$4.02\ 10^{-2}$
1.25	$9.93\ 10^{-2}$
1.50	$3.10\ 10^{-1}$
1.75	$7.65\ 10^{-1}$
2.0	$9.56\ 10^{-1}$

The mass balance for the reaction is given by

$$fC_o = fC - \frac{dO}{dt}$$

where C_o and C are the gas compositions entering and leaving the graphite electrode within the tube and $\frac{dO}{dt}$ is the rate of reaction of the impurities with the graphite. An analysis of the results in the table shows that the rate of reaction is neither first order nor any higher order reaction. This behavior may be expected if the reaction products inhibit the reaction as would be expected for graphite.

No conclusions can be reached at present as further controlled experiments will be conducted. However, this work is pre-

sented to illustrate the possibilities of using oxygen activity measurements to study the reaction of impurities with graphite or the influence of catalytic impurities in the graphite.

Oxygen Activity Meter

An electrolyte cell is being characterized and checked for use in monitoring the oxygen activity of the helium gas. The cell consists of a ZrO_2-Y_2O_3 tube closed on one end with silver film electrodes both on the inside and outside of the tube. The outside of the tube is exposed to air as the reference gas and a stainless steel tube passes down the center of the tube and contacts the silver via a platinum wire mesh. The resistance of the cell has been studied in some detail as a function of temperature. This work was carried out as it affords a method for monitoring the meter itself; possible changes could result from, for example, the evaporation of silver.

The variation of the resistance of the cell was unusual as there was a break in slope on an Arrhenius plot. Above 500°C the activation energy for the conduction process was 29.3 Kcal/g mole, a value in the range of other published data. The break in the curve which occurred between 400 and 500°C had an approximate activation energy of 6.0 Kcal/g mole. Below 400°C the activation energy again increased but the value was low, 16.5 Kcal/g mole. There is at present no explanation for the observed resistance variations. Measurements will be conducted on other cells constructed to determine

if this is a reproducible effect.

The variations of potential of the meter with different oxygen concentrations have been carried out. These measurements are given in Table 2-1 for 650°C. For comparison, calculated or expected potentials are also given. Further work is in progress to determine what factors are responsible for the lack of agreement even though the comparison is reasonable.

Measurements have also been conducted with addition of hydrogen to helium and their effects on the measured oxygen activity. At 650°C with approximately 8.5% H_2 present the measured potential was 1.23 volts giving a hydrogen to water ratio of approximately 2.5×10^2. This value was lower than expected. On saturating the helium plus hydrogen gas with water the potential decreased to 1.04 volts giving a ratio of 3 which was the expected value. Measurements will be conducted with lower water levels controlled by low temperature equilibration of helium containing hydrogen.

C. Fuel Hydrolysis/Oxidation (D. Chandra)

A review of the OXIDE-3 code as it currently exists was carried out with a view to evaluate the experimental basis for the analytical method used to describe the fuel hydrolysis reaction. The following conclusions were drawn:

1. Data used in OXIDE-3 refer principally to ThC_2 or $(Th,U)C_2$ hydrolysis. Only a few data points with UC_2 have been considered. Besides some low temperature (30°C and 50°C) studies, these consist of 4 points at 300°C included in Table Q.7-1 in Amendment 1

Table 2-1

Variation of Oxygen Meter Potential With Oxygen Concentration

Oxygen Concentration Atmospheres	Potential Volts* Observed	Calculated
0.030	37	39
0.035	30	35.5
0.042	24	32
0.053	21	27
0.076	15	20
0.090	14	17

*Reference electrode: air.

of LTR-7. Three of these points refer to irradiated UC_2 (with 30, 25 and 50% burnups) and the fourth to unirradiated UC_2. A marked drop-off in reaction rate was observed with irradiation.

2. No consideration was given to the UC_2-CO reaction under HTGR conditions in OXIDE-3.

3. No consideration was given to the influence of H_2O or CO on fission product transport and distribution.

Currently GA is carrying on investigations on the UC_2-H_2O and UC_2-CO reactions. The main emphasis has been on the UC_2-H_2O reaction. The tests involve exposure of laboratory prepared fuel rods containing known quantities of failed fuel to water vapor at temperatures from 300°C to 900°C. The R/B measurements are performed intermittently during the exposure.

The water concentration used during many of the runs was 100 ppm water at 1 atm total pressure (equivalent to 2 ppm H_2O at 50 atm He). These therefore do not relate to severe water or steam ingress accident conditions where the water levels would be considerably higher. Hydrolysis of bare kernels, according to available GA data, causes a rapid increase in R/B to 40 to 60% within 50 to 100 hours of exposure. The rods prepared from laser drilled particles reached lower R/B maximum (25 to 40%) after 200 to 600 hours of exposure, indicating slower overall hydrolysis rates due to the lower fraction of carbide kernels exposed. The final R/B values after long term exposure are quite similar for the laser-drilled and bare

kernel specimens (~10-16% after 1200 hours, compared with ~4% for unhydrolyzed bare kernels). Though GA has reported significantly lower initial R/B when irradiated fuel kernels were hydrolyzed, the long term R/B values appear to be virtually identical.

The UC_2-CO reaction studies have also been started by GA. They consider that the impurity levels in CO (for example, H_2O, O_2 and CO_2 if any) have much higher reaction rates with the carbide fuel particles than CO. Hence, precautions need to be taken to ensure the absence of these oxidizing impurities. The preliminary data obtained by GA with just CO present show very low reaction rates. Since their studies are still continuing, a request has been made to GA for their latest data.

Two reasons can be cited to justify an independent laboratory evaluation of the importance of CO with regard to the oxidation of UC_2:

1. Apparently there may be a large difference between GA's latest data and results reported earlier in 1974[2-2]. As mentioned earlier, the latest data are not available from GA yet, but this assessment has been made by GA researchers and communicated to us.

2. The influence of hydrogen, specifically the reaction:

$$CO + H_2 = H_2O + C.$$

This reaction becomes thermodynamically possible below ~700°C. It is

the opposite of the steam-carbon reaction. Apparently the presence of a reduced metallic surface catalyzes this reaction[2-3]. Since the water produced in accordance with the equation shown above may lead to considerable hydrolysis, this reaction could be important. The presence of hydrogen itself may also act to catalyze the reaction even in the absence of water.

With this assessment, the following experiments have been planned:

UC_2 With CO

The reaction which will be studied is:

$$UC_2 + 2CO = UO_2 + 4C.$$

Thermodynamic calculations for this reaction show that when the partial pressure of CO is 10^{-3} atm (~20 ppm CO in 50 atm or 1000 ppm CO in 1 atm He), which is twice the design level of oxidizing impurities (~10 ppmv), conversion to oxide will occur at temperatures below ~1340°C. For 200 ppm CO in 50 atm He, the onset temperature is raised to ~1480°C. At low temperatures and low CO concentrations, UC_2 oxidation is feasible. For example, oxidation should occur below 1100°C for CO concentrations approaching 0.1 ppm.

The samples to be used are as follows:

1. Bare, loose, unirradiated VSM UC_2 kernels.
2. Bare, loose, unirradiated W.A.R. kernels with 0%, 15%, 50%, 75% and 100% conversion, respectively.
3. Bare, unirradiated VSM UC_2 kernels in rods.
4. Bare, unirradiated W.A.R. kernels in rods, again with 0%, 15%, 50%, 75% and 100% conversion, respectively.

The extent of reaction will be measured by using a Cahn microbalance capable of measuring weight changes of the order of 10^{-6} grams. Since the UO_2 formed is $\approx$1.03 times heavier than the original UC_2, the balance should be sensitive enough to measure less than ~0.1% reaction for a sample batch of 100 mg of particles.

Following the establishment of the preliminary kinetic behavior by monitoring weight changes as a function of time, two additional methods may be used to determine the extent of reaction: (1) hydrolyzing the remaining UC_2 and measuring the hydrolysis product ethane and (2) standard metallographic techniques.

Apparatus

Construction has begun on the circuit to conduct the oxidation tests (Figure 2-3). Precautions will be taken to remove O_2, CO_2 and water impurities, from the He/CO gas mixture. Accordingly, the gas will be prepurified by passing it through an activated charcoal trap at -78°C to remove the major amounts of water, through an ascarite trap to remove CO_2, through a calcium chloride and a P_2O_5 trap to remove any water taken from the ascarite and through a heated bed of Cu dispersed in graphite to remove O_2.

The oxidation reaction will be carried out inside a quartz tube heated by a furnace. The samples will hang from one side of the microbalance inside the tube in an alumina boat. Temperatures will be measured using a chromel-alumel thermocouple.

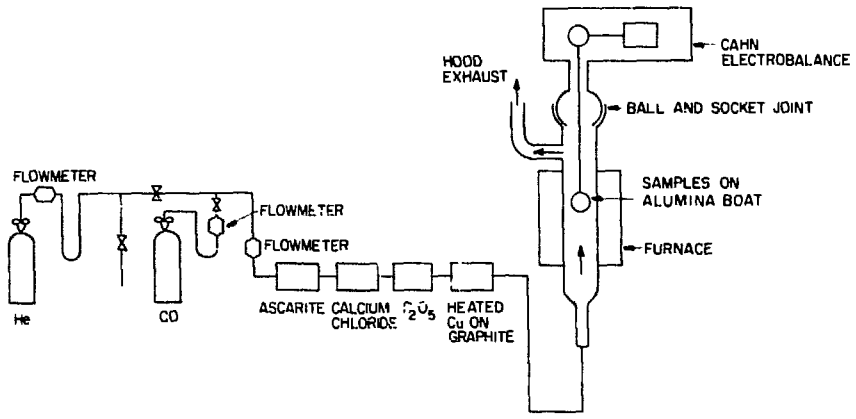

Figure 2-3. Oxidation apparatus.

Sequence of Experiments

Measurements of the reaction kinetics will be conducted as a function of temperature and CO partial pressure for temperature ranges below ~1300°C with 100 mg batches of VSM UC_2 and W.A.R. kernels.

Reaction kinetics as a function of temperature and H_2-CO mixture partial pressure will then be measured. The mixture will consist of equal amounts of H_2 and CO. Some details of this particular experiment are still being evaluated.

After establishment of at least the preliminary kinetic behavior, the influence of CO attack on fission gas release from uncoated particles will begin. Lack of experimental equipment may delay this portion of the program considerably.

UC_2 with H_2O

A similar experimental approach will be followed to study the UC_2-H_2O reaction. For this purpose, water vapor concentrations of 1000 to 20,000 ppmv (in 1 atm total pressure of He) will be employed.

Following establishment of the preliminary kinetic behavior, the effort will be extended to study the attack of the particle coatings by water vapor. Early work by Blakely and Overholser[2-4] indicates this possibility at 990°C even for rather low concentrations of water vapor (500-1000 ppm H_2O in 1 atm He). For this purpose both TRISO and BISO particle batches will be studied. This portion of the program is still in the planning stages.

References

2-1 HTGR Safety Evaluation Division Quarterly Report, April-June 1975, BNL-50460.

2-2 HTGR Base Program Quarterly Progress Report for the period ending February 28, 1974, GA-A12916, UC-77.

2-3 M. R. Everett, D. V. Kinsey and E. Romberg, "Carbon Transport Studies for Helium Cooled High Temperature Reactors," UKAEA Report D.P. 491, November 1966.

2-4 J. E. Baker, L. G. Overholser, "Oxidation of Pyrolytic-Carbon-Coated Fuel Particles by Low Concentrations of Water Vapor," ORNL-TM-2199, April 1968.

III. Rapid Graphite Oxidation

A. Analysis of Impurities in Graphite (A. Romano, J. Forrest)

Two large sections of candidate HTGR core support graphites (ATJ and PGX) have been received from Union Carbide Company for use in our experimental program. The graphites will be used to supply specimens for chemical analysis, oxidation rate measurements, metallographic studies, physical property measurements, and mechanical testing. The ATJ graphite log was sectioned to form two near typical Ft. St. Vrain posts, one of which was further divided into samples for use in a statistical analytical chemistry program.

The purpose of the chemistry program is to develop the analytical data required to determine the impurity distribution profile of a typical ATJ graphite post and to correlate this data with oxidation and strength measurements which will be performed on the second post fabricated from the same log. Further, an attempt will be made to establish the nature, location, and concentration of each of the catalytic species in the graphite matrix. A similar but limited program will be initiated on the PGX graphite. Elements which will be routinely analyzed are Fe, Si, Al, Ca, Mg, Ti, V, Ni, and Mn. Of secondary present interest, but within the realm of possible future analysis are Co, Ag, Mo, B, Cs, Ca, Sr, Li, Pt, Cu, W, Cr, Pb. The number of samples contemplated is of the order of several hundred per month.

Several analytical procedures have been evaluated for performing these analyses. Emission spectroscopy appears to allow the

analysis of the largest number of samples in the shortest period of time when compared to other methods. The technique consists of grinding graphite specimens to a powder, placing a sample into a graphite cupped electrode and burning in a direct current arc. The emitted light is sent into a spectrograph where it is diffracted by a diffraction grating and resolved into characteristic wavelengths of light representing individual elements in the sample. The spectrum is photographed and the resulting plate examined in a densitometer to measure the density of the elemental lines of interest. Line density is converted into source-emitted light intensity by means of emulsion calibration curves. Finally, elemental concentrations are obtained from calibration curves relating light intensity to concentration, via standards.

A direct-reading alternate procedure to photography and densitometry consists of placing exit slits on the spectrograph focal plane at each elemental wavelength of interest. Individual phototube multipliers behind each slit convert light energy into electrical energy. A high speed digital readout system accumulates and stores the phototube multiplier output current on capacitors, one for each element simultaneously. In addition, the readout controls timing of various spectrometer operations. During measurement, unknown voltage is automatically ratioed against a reference or matrix voltage. It is then converted to a digital number, which is logarithmically related to element concentration.

The Analytical Chemistry Group presently posseses a Baird

Model GX1-125 spectrograph with a clock console readout system employed in the photographic mode. With some slight repairs, the spectrograph itself could be adapted to the digitized system described above. It is proposed to purchase the Baird-Atomic high speed digital readout and Spectrocomp system as additions to our present Baird spectrograph. The Spectrocomp system, consisting of a Digital Equipment Corporation PDP-S/M computer, control panel, interface and teletype converts digital readout to element concentrations, which are printed directly in percentage. Standardization is automatically accomplished and calibration curves are stored in memory. The proper working curves are selected, corrections are made for background and results averaged. Results of a run can be rejected and another run made. A complete quantitative analysis can be obtained within 1-2 minutes.

B. Possible Combustion Hazards of HTGR'S (A. L. Berlad, State University of New York at Stony Brook; H. B. Palmer, Pennsylvania State University; M. Sibulkin, Brown University; R. A. Strehlow, University of Illinois; C. H. Yang, State University of New York at Stony Brook)

In the event of steam leakage or air ingress into the prestressed concrete reactor vessel (PCRV) of a high temperature gas cooled reactor (HTGR) reaction between the graphite and the steam or air produces combustible gases which contain H_2 and/or CO. When these gases are mixed with air various destructive modes of combustion, such as flame, explosion and detonation, may occur. The present report examines some circumstances under which combustion accidents may present a threat to the safety of the reactor environment. Discussions are also extended to the physical characteristics and potential destructive power associated with these phenomena.

It is estimated that a containment building of a 3000 MW HTGR at $100^{o}F$ contains 5185 lb moles of air. Suppose 20% is oxygen. We shall have 1090 lb moles of O_2. Let half of it react with graphite; 1090 lb moles of CO will then be produced. The total amount of He contained in the PCRV is 5250 lb moles. If all these gases are homogeneously mixed we shall have a mixture with 5.0% O_2, 9.9% CO, 37.3% N_2 and 47.8% He. This is not a flammable mixture according to Coward and Jones' data[3-1]. On the other hand if He is not mixed with the rest of the gases we would have a mixture with 19% CO, 9.5% O_2 and 71.5% N_2. This obviously is a flammable mixture. However, it is not capable of supporting a destructive detonation wave. The mixing

processes of the fuel gases produced in the HTGR in the course of an accident, therefore, are of great importance in determining the combustion hazards. We shall consider some physically plausible situations under which poor mixing or layering of gases may occur and favorable conditions for combustion phenomena created.

Combustion Hazards Resulting From Rapid PCRV Depressurization

In a report[3-2] prepared by General Atomic Company to provide information regarding postulated accidents, an event of rapid PCRV depressurization was considered. One of the important factors the report neglected to cover is the possibility of layering of gases after the depressurization. A simple but quantitative analysis will now be presented to show that gas layering is quite likely and that a combustion accident may follow and be damaging to the reactor environment.

Gas Layering in the Containment Building

The model of gas layering in the containment building after a blowdown accident is formulated with the following assumptions:

1. The leak is located on the top of the PCRV with an opening area of 100 in^2.

2. The egress of pressurized He into the containment building is assumed to be an adiabatic process.

3. The containment building does not leak and there is no substantial circulation in the building

4. All gases obey the ideal gas law.

To check the possibility of layering, three separate calculations were performed to determine the "final state" of the system. "Final state" is defined as the gas state immediately after the blowdown. A later "after cooling" state was also considered. The three limiting cases considered are:

1. No mixing of He and air (i.e. complete layering).

2. Complete mixing of all the He and air that is in the containment building (i.e. no layering).

3. At the final state all the gas below the upper surface is pure air, while all the gas above this surface is a fully mixed mixture of He and air (i.e. one example of partial layering).

Calculated results are presented in Table 3-1.

The results given in Table 3-1 under the column heading "After Cooling" were calculated under the assumption that gases were cooled to the initial ambient temperature of $100^{o}F$. The density ratios relative to air for the different gases or gas mixtures as well as the location of the layered levels above the PCRV upper surfaces are also calculated. Figure 3-1 shows the relative position of the interface in the containment building for the final state of case.

The three calculated cases should be regarded as pure limit cases and are intended only to illustrate the point that layering must occur in the containment building during the initial blowdown phase for an upper surface leak.

Table 3-1

Calculation of "Final State" of the System and for After Cooling

Case		Final State					After Cooling		
		P_f atm	T^oR	MW	$\frac{\rho_{Air}}{\rho_{He\ Mix}}$	Layer Height Above PCRV	$\frac{\rho_{Air}}{\rho_{He\ Mix}}$	Layer Height Above PCRV	$\frac{\rho_{Air}}{\rho_{Egress\ Gas}}$
No mixing	He layer	3.00	960.5	4	9.08	36.6'	7.24	46.3'	1.44
	Air layer		765.9	28.965					
Full mixing	He + Air	2.92	836.5	---	---	---	---	---	---
Partial mixing	He + Air layer	2.95	881.0	12.21	2.74	0.0'	2.37	4.7'	1.44
	Air layer		762.3	28.965					

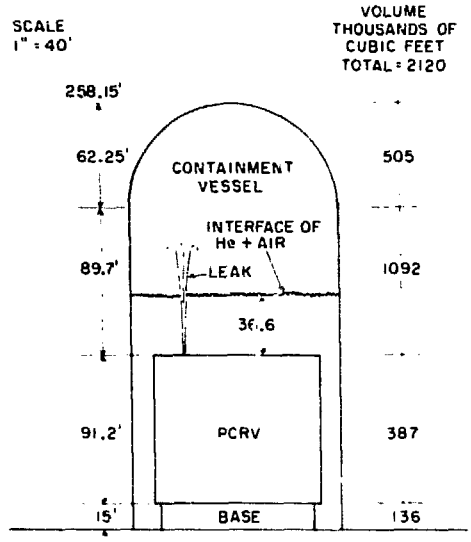

Figure 3-1. The PCRV and containment vessel geometry.

Major arguments for layering can be summarized as follows:

1. The leak is small, relative to the size of the containment building. A 100 in^2 opening is equivalent to a circular area with a diameter of 0.94 feet. The leak is at least 100 feet below the ceiling. Thus one would expect that virtually all of the initial jet momentum would be lost before reaching the ceiling. Air entrainment into the jet would be the only mixing mechanism. A straight upward jet would not impart much swirl or other types of gross mixing motion to the contents of the containment building.

2. The density ratio (Table 3-1) for no mixing is large (7.24) and no matter how much local mixing occurs, layering will persist. Since blowdown lasts only about 5-10 minutes a distinctly layered quiescent gas mixture in the containment building is expected 20 minutes after the start of the blowdown. After the

gases become quiescent, diffusion-controlled mixing will be ineffective in creating a homogeneous gas mixture in a space of this size. Cooling at the wall will cause some convective flow and accelerate the mixing process but layering will slow this process.

In general, cases 1 and 3 may be considered as good approximations to the limit behavior of the system. No effective mechanism is conceivable to provide the mixing of air at the sides of the PCRV. Compression by the released coolant gas will, of course, move some of the air from above the PCRV down the sides, but there should be only traces of helium in this air. The major fraction of the air entrained by the jet will simply remain near the ceiling of the containment building. Upon cooling, this gas will pour over the top of the PCRV because the gas above is considerably hotter at the end of blowdown. This may cause the PCRV to ingest pure air and later release a CO-N_2 mixture to the containment building.

A considerably more sophisticated approach to the present calculation can be made. Jet mixing processes with ambient air entrainment may be considered in such a mixing model. Reaction kinetics for the CO-N_2 gas reaction with air may be added as these gases leave the PCRV to enter the containment building. The present simple illustration, however, has established the strong tendency for layering during PCRV blowdown.

Accumulation and Release of Combustible Gases

Air may enter the PCRV through natural convection and "contraction," as pointed out in reference 3-2 for the case of a simple leak at the top. With layering, pure air will be ingested into the

PCRV. In case of complete layering the amount of air above the top surface of the PCRV is 46% of the total. Assuming 40% of it is ingested and reacts with graphite the amount of CO that may be released comes to 872 lb moles. If the CO is released at the bottom of the PCRV and mixes with the layered pure air one has a mixture with 11.6% O_2, 15.6% CO and 72.9% N_2. This is a flammable mixture. For a PCRV generated mixture 30% CO and 70% N_2 entering the air layer in the containment building the evolution of the composition of the effluent is shown by a dotted path in Figure 3-2. It is well within the flam-

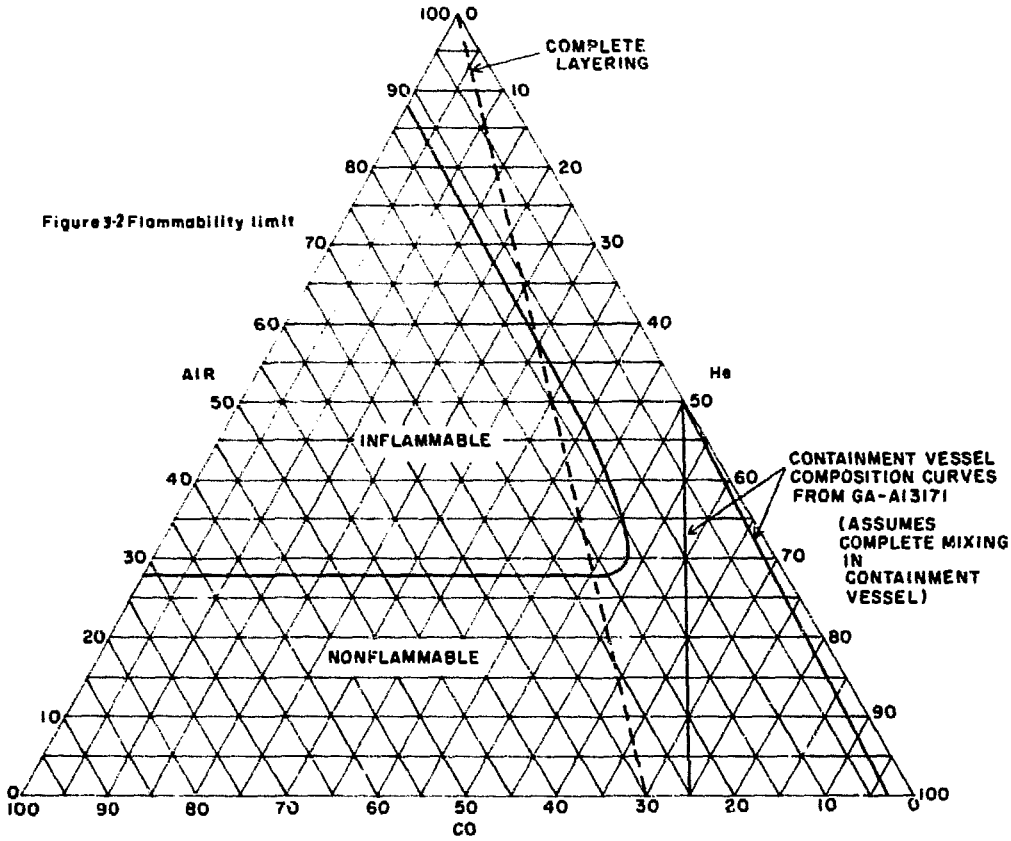

Figure 3-2. Flammability limit.

mability region. Localized flame combustion, therefore is quite possible.

We may consider an accident in which a large opening (100 in^2) on the top of the PCRV and a small opening ($\leq$10 in^2) at the bottom simultaneously develop. The layering pattern of the gases will not be substantially different from that given above, due to the fact that the effluent flow from the small opening will be only a very small fraction of the total. Slow convective flow after the blowdown may enter the PCRV through the small opening below and depart from the top. Circulation of this type will provide the mechanism for generating CO gases and mixing with the layered air discussed in the preceding section.

In the postulated depressurization accident concurrent with a steam leak reference 3-2 estimated the total water ingress to be 3179 lb. If all of it is allowed to react with graphite a total number of 353 lb moles of equal amounts of H_2 and CO will be produced. Mixing of these gases with the layered air at the lower portion of the containment building yields a mixture with 3% H_2, 3% CO, 19.7% O_2 and 74.3% N_2. This is approximately at the lower limit of flammability of the mixture according to reference 3-1. The amount of H_2 and CO depends largely on the amount of water ingress and the temperature of the core during the cooling period of the PCRV. It is not unreasonable to assume that the mixture may be even richer under some circumstances (for example, if the steam is not cut off) and becomes more flammable. In this case only one opening is needed for the fuel gases to enter

the containment building but the circulation with the two openings postulated previously will work equally well.

Consequences of Combustion Hazards

Of all the combustion modes that may occur, probably spontaneous explosion is the least likely. Uneven distribution of temperature and the presence of ignition sources will almost certainly force the combustion mode to wave phenomena rather than homogeneous explosions (autoignition). The most likely mode of combustion is probably flame propagation through a premixed mixture. Some characteristics of the various modes of combustion are now discussed:

Premixed Flames

Flames propagating in a premixed mixture generally are not associated with sharp pressure peaks. An overpressure may be associated with the transient period of flame initiation. This usually does scarcely any damage. The situation is quite different when the flame system is confined within a sealed container. The final pressure in the container may rise several fold after the passage of the flame and the release of chemical enthalpy. When the flame system occupies only a portion of the container the calculable pressure rise will be less severe. Consider the case where the leak is located on the top of the PCRV with an opening area of 100 in. Let the pressure in the containment building after the blowdown be approximately two atmospheres. Since the combustible mixture occupies approximately 50% of the total space it is obvious that the pressure will be more than doubled after a flame propagates through it. This

overpressure, undoubtedly, would exceed the present design strength of the containment building.

Flames supported by a small plume of combustible gases will, of course, be far less harmful. This is alluded to in reference 3-2. A thorough analysis of this type of phenomenon is needed.

Diffusion Flames

Fuel (H_2 and/or CO) and inert (He and/or N_2) mixtures issuing as a jet into ambient air may support a diffusion flame stabilized at the exit. In either of the two previously discussed cases, (1) and (2) under Gas Layering in the Containment Building, a possibility exists that a diffusion flame may be stabilized at the opening where the combustible gases enter the containment building. As energy is released by the diffusion flame the pressure is, of course, expected to rise. The persistent local heating by the flame may also undermine the neighboring structural members and instruments. Fortunately, for such a diffusion flame to exist the fuel concentration in the jet must be very high. Usually the required fuel concentration is much higher than the lower flammability limits of premixed flames for the same fuel. For instance, the leanest mixture of hydrogen and He that will burn when issued as a jet into ambient air is 14% H_2 and 86% He. The lower flammability limit for an air and H_2 mixture is only 4% H_2. The possibility of a diffusion flame in a blowdown accident probably still deserves to be closely examined.

Detonation

Detonations in gaseous media usually occur in confined narrow spaces, such as metal tubes. This type of detonation wave usually consists of a leading plane shockwave followed by intense chemical reaction. In large geometric spaces without pressure confinement only a spherical type of detonation wave may be initiated. Spherical detonation wave initiation generally requires a powerful source with a very fast energy release rate. Condensed explosives, lasers and powerful electric discharges have been successfully used to induce spherical detonation in laboratory experiments[3-3 to 3-5]. The detonability limits for spherical detonations are believed to be much narrower than the limits for plane waves in tubes. Experimental data for this phenomenon are extremely scarce.

Strehlow[3-6] has surveyed the records of unconfined vapor-cloud explosions that have occurred in the past 42 years. Only one case was found that might have been a detonation. If detonations are considered to be real possibilities in the HTGR, they must be carefully studied. With many ignition sources available in a reactor environment mixtures are probably consumed by flames long before they can reach the stoichiometries necessary to support spherical detonations. The probability of detonation thus is slim.

References

3-1 H. F. Coward and G. W. Jones, "Limits of Flammability of Gases and Vapors." U. S. Bureau of Mines Bulletin 503, 1952.

3-2 General Atomic Standard Safety Analysis Report, Chapter 15. General Atomic Company, San Diego, California.

3-3 G. G. Bach, R. Khystantas and J. H. Lee. XII International Symposium on Combustion, p. 853 (1969).

3-4 H. Freiwald and H. W. Koch. IX International Symposium on Combustion, p. 275 (1963).

3-5 E. L. Litchfield, M. H. Hay and D. R. Forshey. IX International Symposium on Combustion, p. 282 (1963).

3-6 R. A. Strehlow. XIV International Symposium on Combustion, p. 1189 (1973).

IV. Structural Evaluation

A. Structural Analysis (M. Reich, P. Bezler, T. Y. Chang, B. Koplik, J. R. Curreri, L. Laske)

The primary efforts during this report period were made in the areas of core seismic response and core and core support structures. Results of these investigations are detailed in the sections that follow. In addition, work pertaining to the PCRV and liner is also being continued. This effort is still in the formative stages and a report outlining the progress should be available for the next report period.

Abstracts of two papers entitled respectively, "Non-Linear Dynamic Response of a Multi-Element HTGR Core Structure" and "One Dimensional Spring-Mass System for Seismic Analysis of HTGR Core" were submitted to the Second National Symposium on Computerized Structural Analysis and Design to be held in Washington, D. C. late in March of 1976. The report describing the BNL Horizontal Array Seismic Code OSCIL[4-1] is currently in press and will be released as soon as it becomes available.

Core Seismic

The parametric study for the horizontal array model shown in Figure 4-1, has led to significant results for the system's dynamic response. Based on the computer program, OSCIL[4-1], which was specifically developed to solve for the response of this model, results were obtained regarding the effects of mass lumping and clearance for various input motions. The graphical strip chart of the PCRV vessel inputs as well as core response outputs are shown

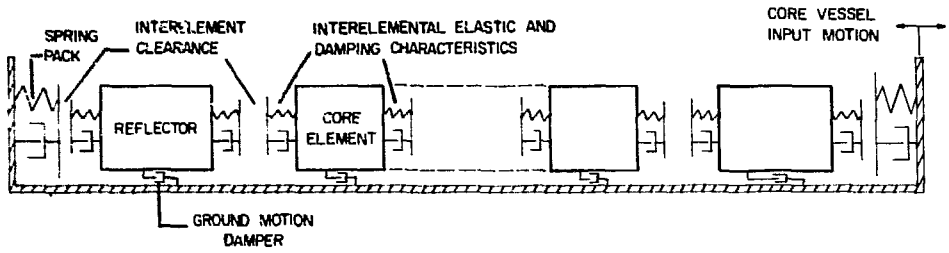

Figure 4-1. "N" mass model.

in Figures 4-2 to 4-5.

In interpreting these figures, the strip (or long axis) is the time coordinate while the dimension across the strip (the short axis) is the individual displacement of the mass point. Each mass is given by a single trace. Where the clearance between adjacent mass points goes to zero, a single trace then shows the path of the clumped masses. In all the strip chart plots the two boundary, or outermost, traces represent the input vessel motions.

Figure 4-2 depicts the response obtained from OSCIL for various lumped mass representations of the system. As can be seen from the figure, the starting transients of the displacement-time-histories for 5, 7, 9, and 30 mass systems are plotted. The total mass, total clearance, interelemental damping factors, forcing frequency and amplitude are all held constant for these runs. In all four cases the initial response is quite similar with collisions taking place from left to right until some degree of clumping occurs. The clumping characteristic is revealed as the mass points approach each other. As the space between elements diminishes the plotting tends towards a single trace. Although this characteristic repeats itself, separation of the elements is apparent between the clumping intervals, with different response characteristics shown for the several mass models analyzed.

Figure 4-3 shows the same mass systems being excited at their resonant frequency (or frequency of maximum response). As can be seen from this figure, the response of all mass systems have similar

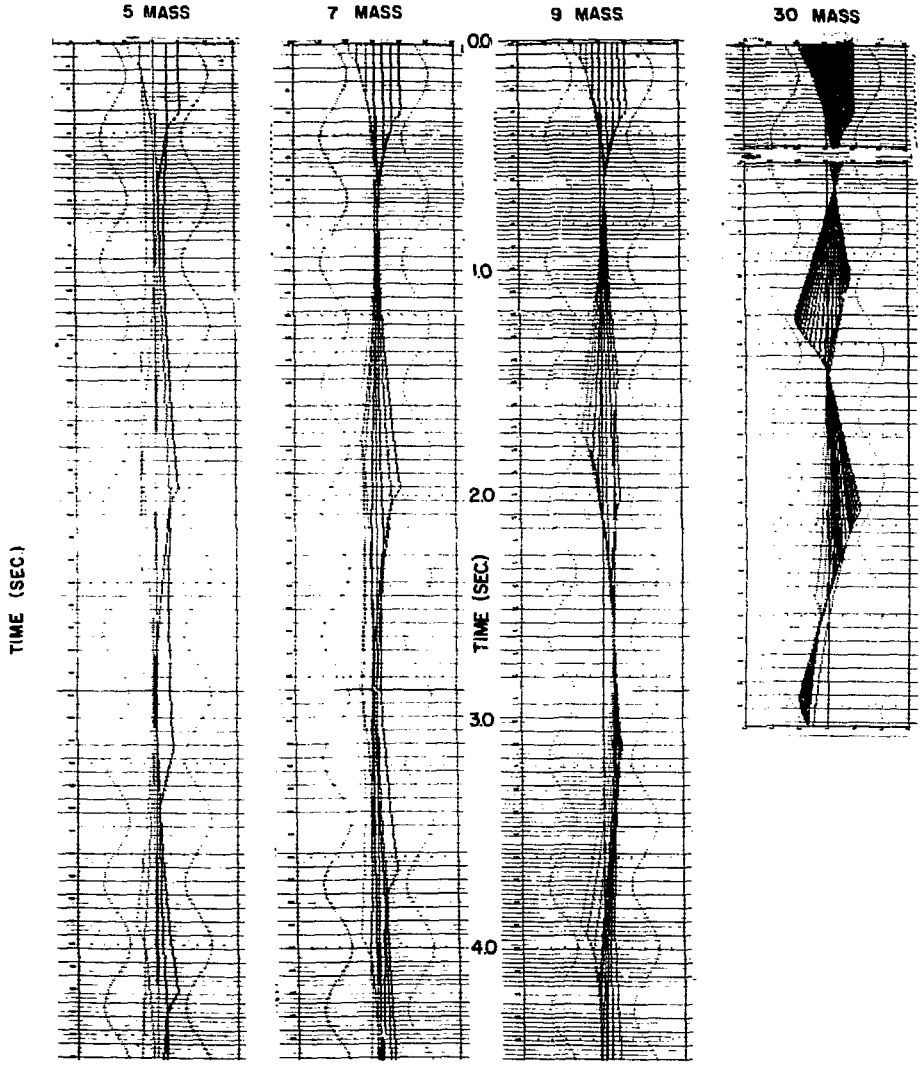

Figure 4-2. Dynamic response of different mass models at 11.4 $\frac{\text{rad.}}{\text{sec.}}$.

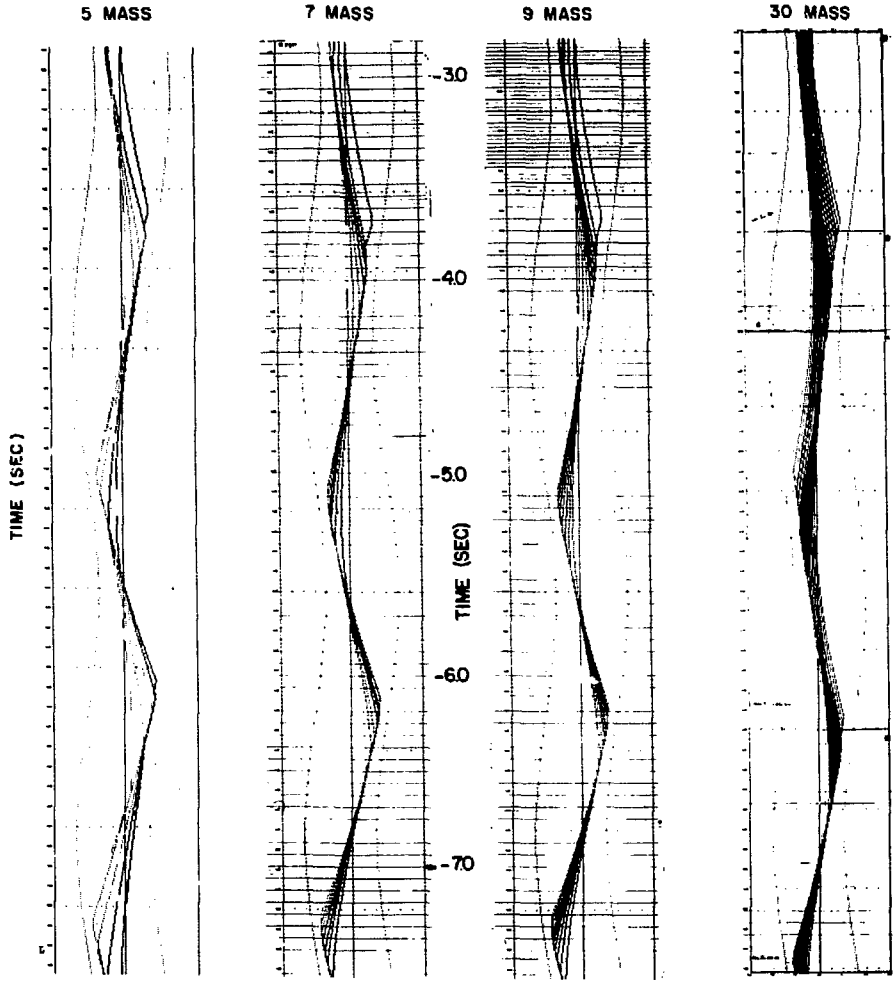

Figure 4-3. Dynamic response of different mass models at resonance.

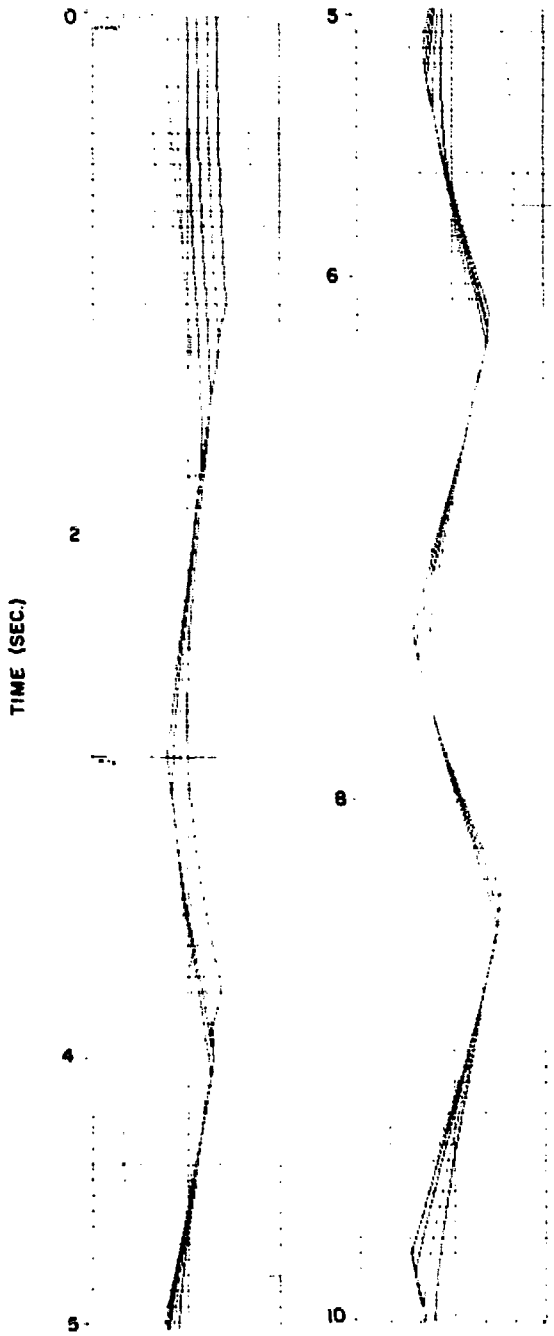

Figure 4-4a. Resonant response of 7 mass model.

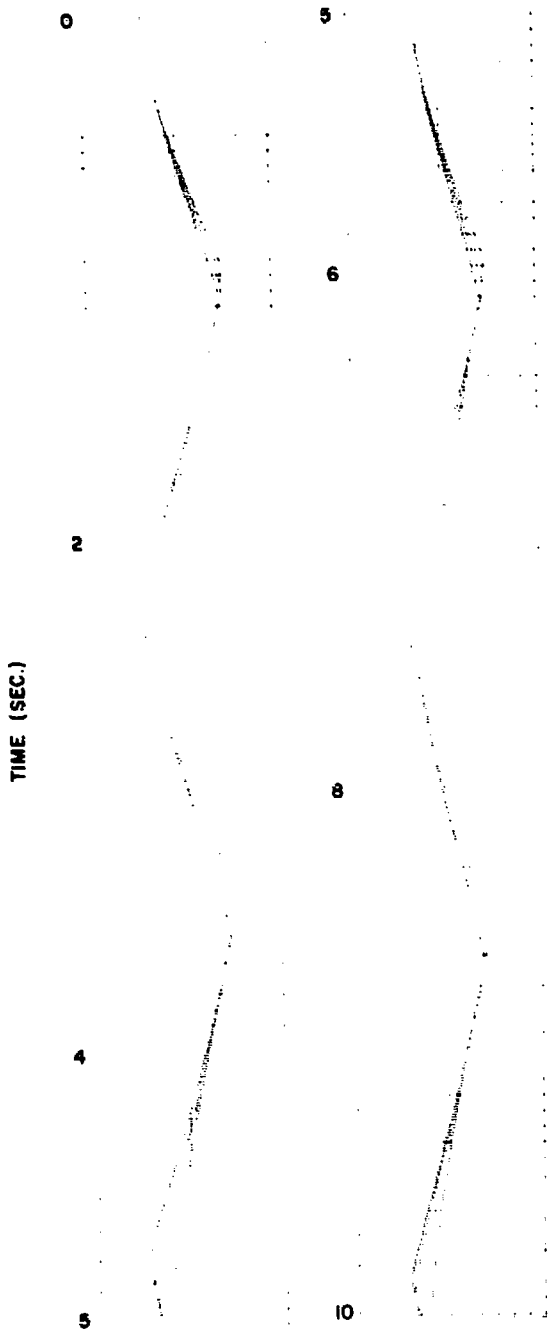

Figure 4-4b. Resonant response of 7 mass model for zero intial spacing of masses.

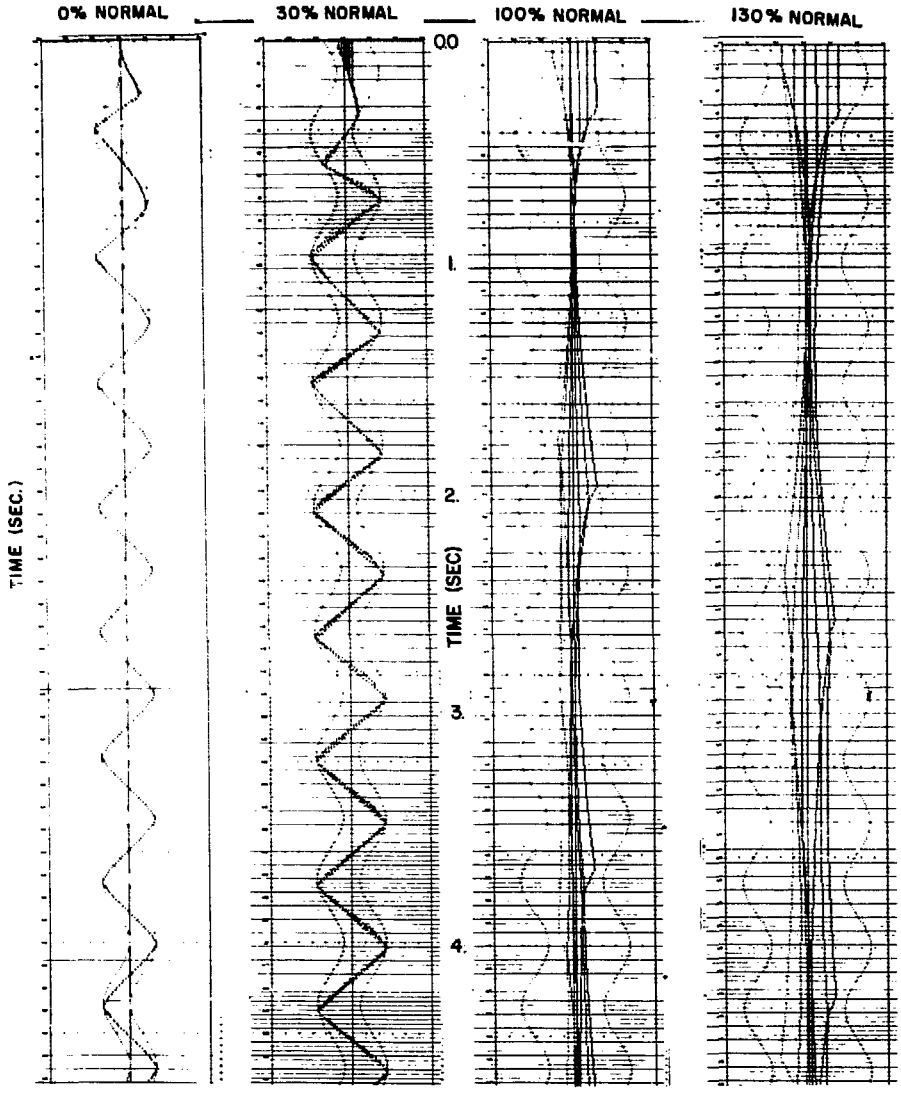

Figure 4-5. Effect of clearance on dynamic response of 7 mass model.

characteristics. Indeed, under the conditions stated above, the five mass system has the same natural frequency as the thirty mass system. In addition, an examination of the forces developed at the wall of the vessel shows that the maximum forces are the same for each of the mass representations. This leads to an important conclusion; that a reduced mass model can be used to represent the dynamic response and transmitted forces of the more complex system even though the problem is highly non-linear.

Figures 4-4a and 4-4b show extended time runs, up to 10 seconds, for a seven mass model starting with two different initial positions of the masses. In Figure 4-4a, the total clearance is initially equally distributed between the mass points. In Figure 4-4b, all of the masses are initially pushed to the left against the left wall spring pack. Both runs are at the resonant frequency. It is seen that in less than 10 seconds the initial transients have largely disappeared and the same steady state motion is obtained for both cases. This clearly demonstrates the insensitivity of the steady state response to the distribution of clearance between masses as long as the total clearance remains unaltered.

Figure 4-5 depicts the effect of varying total clearance when all other parameters including the input forcing frequency are held constant. A seven mass model is used in this case. For zero clearance the seven masses remain clumped and behave as a single mass responding at close to a resonant condition. As the clearance increases to 30% of nominal only slight departures from clumping are revealed and the system is still in the vicinity of resonance.

For both of these cases large forces are developed as the combined mass approaches the walls. The response is highly non-linear and as could be expected there is a broad frequency band over which large forces are developed. When clearance is increased to nominal or 130% of nominal, the plot shows a significant reduction in clumping and in the approach of the internal masses to the walls as well as a reduction in natural frequency of the system to a value considerably below the constant input frequency of 11.4 rad/sec.

Figure 4-6 shows the resonant frequency as a function of clearance for the seven mass model. This frequency characteristic is for a spring pack in which the hard stop is eliminated. As is expected, increasing the clearance reduces the resonant frequency. For this case, an estimate was obtained by an analytical iterative scheme which involved considering the system as piecewise linear and lumping the masses. The time required to traverse each linear interval was superimposed to obtain the total period. The results of this procedure are also plotted in Figure 4-6. Since the total clearance changes due to induced irradiation of the core elements during their operational lifetime, a knowledge of the influence of clearance on the forces acting on the elements during a seismic event is extremely important.

A more realistic representation of damping in the horizontal

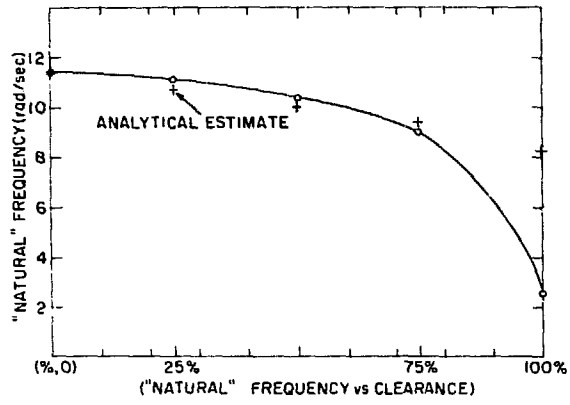

Figure 4-6.

array has been obtained by introducing coulomb damping instead of an equivalent viscous damping at the base of the elements. The results of this study show that although the natural frequency of the system remains unchanged, the dynamic response differs depending on the level of the input forcing function. As the input force increases the response with coulomb damping also increases. However, as the amplitude of the input force decreases the response with coulomb damping decreases such that at low force inputs there is no noticeable response at all.

The development of the multi-element vertical array code is near completion. The code is designed to predict the response of a single stack of "n" blocks when subjected to the simultaneous action of horizontal and vertical forcing functions. Each block element has the three degrees of freedom associated with motions in a plane; horizontal, vertical and rotational. Non-linear gaped springs, coulomb friction between elements and dowel pin interaction effects are included.

Using an early version of this code an evaluation of the characteristics of a single "rocking" block was undertaken. Specifically the response of the block when subjected to harmonic horizontal excitation of the boundaries, the forcing frequency being swept up or down, was determined. This was done for block initial displacements of zero and a finite value. The results are shown in Figure 4-7.

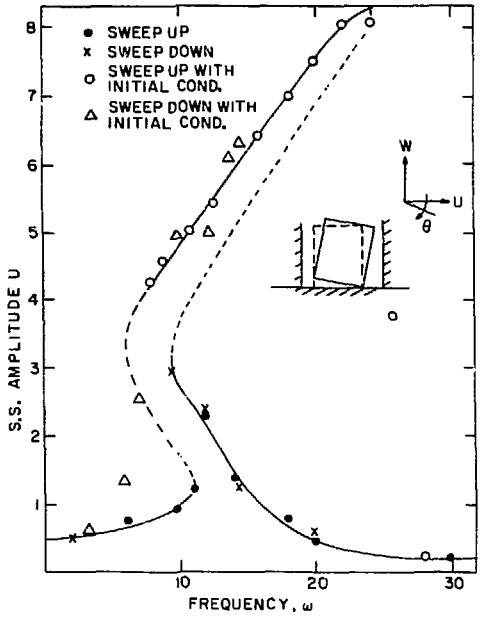

Figure 4-7.

The response curve is typical of a non-linear system having a softening-hardening spring characteristic. For the block it was anticipated that the system spring constant would demonstrate softening as the block rotates onto a base corner and then stiffening as an upper corner makes contact with a vertical boundary. Although a true characteristic of the system, the hardening effect was not evident in the runs starting from zero initial conditions (refer to open dots and crosses on Figure 4-7). Only with initial conditions sufficient to cause upper corner contacts did the characteristic become apparent (refer to circled dots and crosses on Figure 4-7).

Also using the early code version some investigations of a two block array were made. These runs were chosen to test code features rather than to reflect true system characteristics. Figure 4-8 shows the computer generated output for a typical free vibration run. What is shown is a plot of the angles of rotation of the upper and lower blocks vs. time resulting from initial conditions of θ_2 = 0.1 rad and θ_1 = 0.0 rad. As indicated the blocks join following the initial impact and continue to rock as a unit. This motion was expected as the interelemental damping was taken exceedingly large.

Concurrent with the code development work a general investigation of non-linear system response to a seismic event was initiated. The seismic excitation to the HTGR core comes from spectral information. Since the structure is non-linear, a time histo y must be

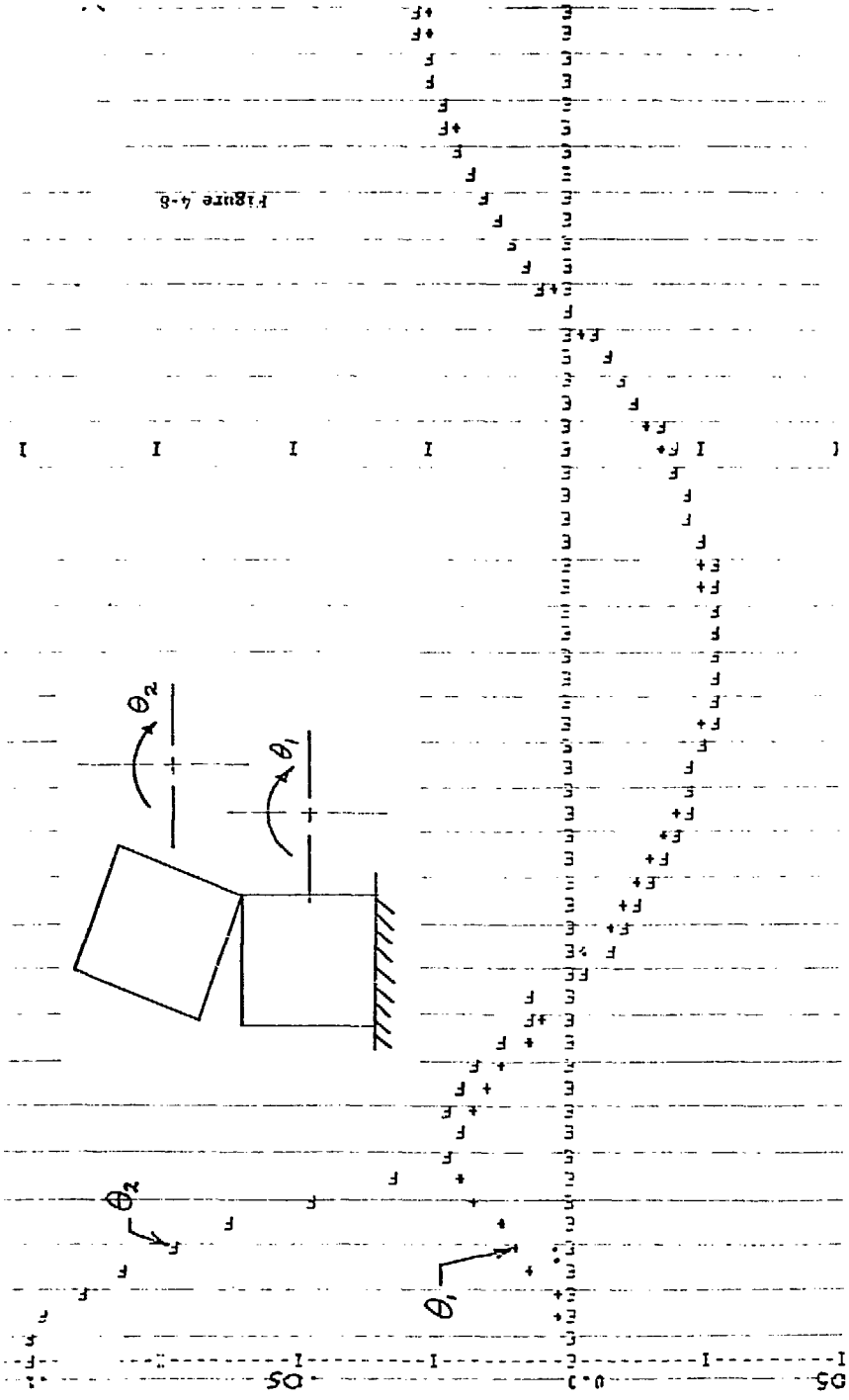

Figure 4-8.

generated which is compatible with the response spectra of the PCRV or of the site, the time history becomes the input to the system. Since there is no unique decomposition in this process, various time histories could be obtained to satisfy the envelope of the response spectra. These time histories can be expressed in a Fourier series with various contributions from different harmonics.

In the literature there is very little information on the effects of simultaneously imposing more than one sine wave on a non-linear system. To gain some insight on the possible choices and the consequences of such a choice in terms of responses that are obtained, two harmonics were simultaneously imposed on a system with cubic elasticity defined by the equation:

$$m\ddot{x} + c\dot{x} + \alpha x + \beta x^3 = f(t)$$

where f(t) is one or more sine waves. The input frequency is swept upwards across the spectrum of interest.

The dynamic analysis of a block model of the core structure has shown that a subharmonic response could easily be revealed for harmonic inputs. These responses develop quite quickly, in just a few cycles of the input and do not require long periods of excitation. With cubic elasticity, a subharmonic could be excited by putting energy into the third harmonic component of the motion. Therefore, our investigation includes a forcing function which is composed of two sine waves with a frequency ratio of three to one.

Figure 4-9 is a plot of the response where $f(t) = 5 \cos \omega t$ -

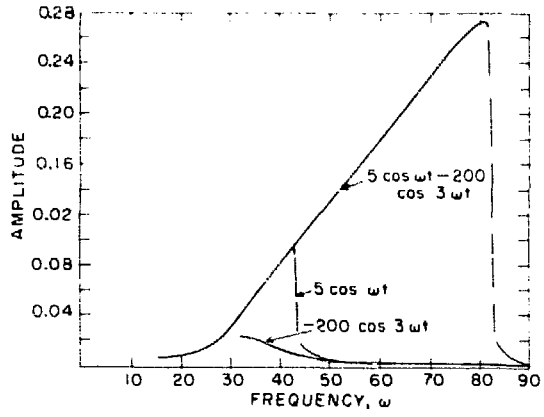

Figure 4-9.

200 cos 3 ωt. The response is shown for each term acting separately as well as for both terms acting together. Notice that the maximum response when both act together is several times the magnitude of when each acts separately. In fact, the response due to 200 cos 3 ωt is very small when it acts by itself. This is because the third harmonic component of the response motion is entirely too small in this case for the cos 3 ωt term to be capable of adding any significant energy to the system.

Figure 4-10 is a plot of the response where f(t) is still 5 cos ωt - 200 cos 3 ωt. However, the range of sweep starts at a lower frequency. The maximum magnitude in this case is about seven times higher than if each one acts separately, but the sine sweep starts at 10 rad/sec instead of 30 rad/sec. This time, the effect is largely due to harmonic excitation due to the cos 3 ωt term.

Figure 4-11 shows that there is a minimum magnitude needed for the subharmonic to be capable of excitation. These curves amplify the information in Figure 4-9 and are for the same sweep

frequency range. The difference in this case is that the coefficient of the fundamental is reduced. Notice that when the amplitude of the fundamental is 0.6 or less, no subharmonic response is obtained. Raising the fundamental amplitude to 0.8 now excites the subharmonic response and results in substantial response amplitudes. The amplitude that develops at 0.8 input is about 0.24 inches while at 0.6 input, the amplitude never is higher than 0.03 inches. In

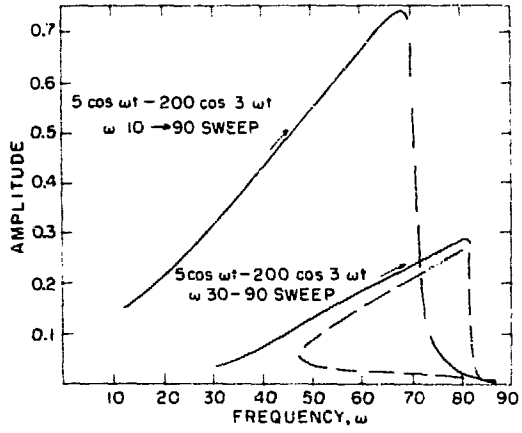

Figure 4-10.

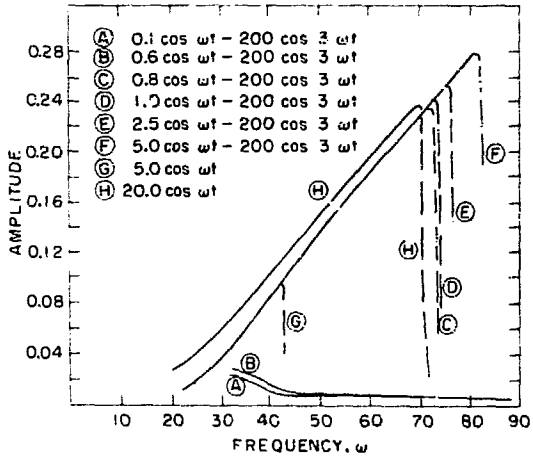

Figure 4-11.

addition, all of the curves that are excited by subharmonic response follow the same path as the frequency is swept up from 30 rad/sec to above 70 rad/sec. The response then drops off to the lower stable root at different frequencies, depending on the magnitude of the first coefficient.

Figure 4-12 shows that phase also has an effect. Curves (1) and (2) are for the same inputs, except that the coefficient of cos 3 ωt is negative instead of positive. The effect of phasing is to cause the response to drop at a different frequency, with a corresponding change in amplitude.

Thus, it is seen that the selection of a particular time history could have a significant effect on the response of a non-linear system. Prior knowledge of the system's characteristics provides guidance in evaluating the most likely choices for generating a worse response.

The design and construction of a horizontal array shake table test jig is nearly complete. The jig is designed to accept 25" long by 4" wide graphite block arrays as shown in Figure 4-13. Variable length spring pack ends are affixed providing the means to vary clearance gaps and simulate core spring pack characteristics. Four graphite block arrays have been machined for initial operations. They will be used to simulate 5, 7, 9, and 11 core mass models. Provisions have also been made to permit an interconnection of the two outermost blocks. This feature will be used to investigate core dynamics with a rigid link between core reflector blocks.

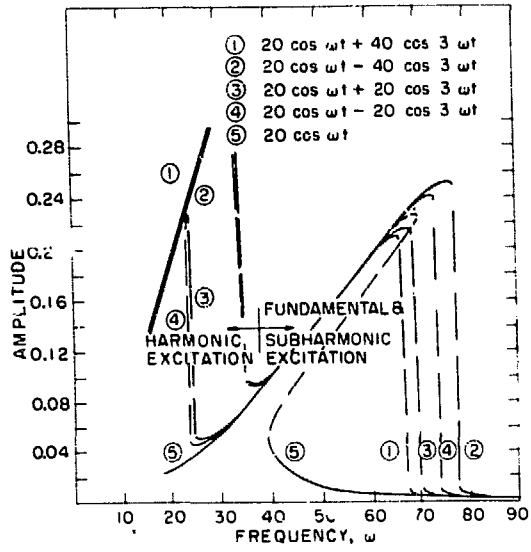

Figure 4-12.

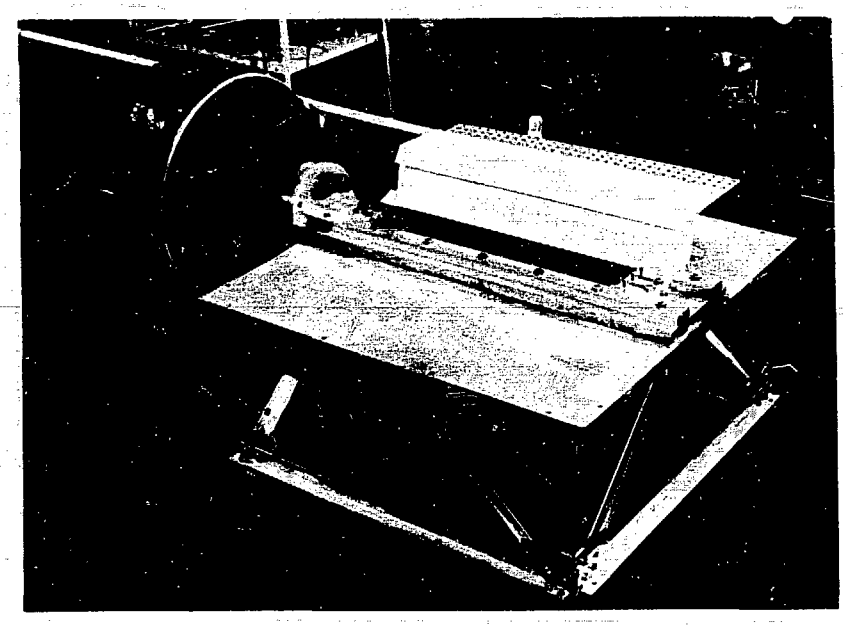

Figure 4-13. Horizontal array shake table test assembly.

Core and Core Support Structures

A finite element program is being prepared to determine the load carrying capacity and corresponding failure modes of HTGR graphite components. To conduct such analyses, non-linear stress-strain relations and cracking of graphite during overloading must be considered. Thus far, only the non-linear stress-strain law for graphite has been developed and it is being implemented into a non-linear finite element program to conduct inelastic analysis for two-dimensional graphite structures. Cracking analysis will be included as soon as the inelastic analysis part is completed. An outline of the stress-strain model used for graphite is described below.

The study of non-linear stress-strain relations for graphite under multi-axial stress state is not abundant. Only some investigations have been carried out in recent years. For example, Greenstreet[4-2] proposed an incremental stress-strain law for artificial graphites under loading and unloading and his theory was merely verified for graphite-G material subjected to biaxial tension[4-3]. Weng[4-4] applied a deformation theory of plasticity to develop a non-linear stress-strain law, and this relationship is known to be valid only for graphite subjected to proportional loading. More recently, Jones and Nelson[4-5] proposed a stress-strain model for graphite which has the same form as for an elastic material except that the moduli in the material matrix are functions of the strain energy. Jones' model

is, in fact, an extension of Weng's model and therefore it is also subjected to the limitation of proportional loading.

From the literature survey, it was found that every little study, either experimental or theoretical, on the stress-strain behavior of graphite has been done and therefore additional work in this area is needed.

At the present time, we are adopting an elastic-plastic model, similar to Greenstreet's approach, to represent the stress-strain response of graphite. Two strain-hardening rules are used in the stress-strain formulations; these are the isotropic and kinematic hardening rules. For the isotropic hardening rule, the yield criterion of graphite has the expression

$$f(\sigma_k) = a_{ij}\,\sigma_i\,\sigma_j - k^2 = 0 \qquad (1)$$

where σ_i is the contracted notation of the stress tensor; a_{ij} are the material constants and for transversely isotropic material they have the form

$$[a_{ij}] = \begin{bmatrix} a_{11} & a_{12} & a_{13} & 0 & 0 & 0 \\ & a_{11} & a_{13} & 0 & 0 & 0 \\ & & a_{33} & 0 & 0 & 0 \\ & & & a_{44} & 0 & 0 \\ \text{symmetric} & & & & a_{44} & 0 \\ & & & & & 2(a_{11}-a_{12}) \end{bmatrix} \qquad (2)$$

The parameter k may be defined as the effective stress, which is

assumed to be a function of plastic work, i.e.

$$k = k\ (W_p) \tag{3}$$

$$W_p = \int \sigma_i\ d\epsilon_i^P \tag{4}$$

Based on the yield criterion, Eq. (1), one can derive the incremental stress-strain law with the assumption of isotropic hardening

$$d\sigma_i = C_{ij}^{EP}\ d\epsilon_j \tag{5}$$

where C_{ij}^{EP} represents the elastic-plastic stiffness coefficient and is given by

$$C_{ij}^{EP} = C_{ij} - \frac{C_{ik}\frac{\partial f}{\partial \sigma_k}\frac{\partial f}{\partial \sigma_\ell}C_{\ell j}}{C_{mn}\frac{\partial f}{\partial \sigma_m}\frac{\partial f}{\partial \sigma_n} - \frac{\partial f}{\partial \sigma_m}\frac{\partial f}{\partial \epsilon_m^P}} \tag{6}$$

C_{ij} is the elastic stiffness coefficient of graphite.

For the kinematic hardening rule, the yield criterion is assumed to be

$$f\ (\sigma_k) = a_{ij}\ \sigma_i'\ \sigma_j' - k_o^2 = 0 \tag{7}$$

and

$$\sigma_i' = \sigma_i - \alpha_i \tag{8}$$

where α_i is the translation tensor of stress and its incremental value is assumed to be given by

$$d\alpha_i = \beta_{ik}\ d\epsilon_k^P \tag{9}$$

In the above equation, the coefficient β_{ik} is permitted to vary as a

function of the stress components as well as loading cycles. Based on Eq. (7), one can derive the incremental stress-strain law for kinematic hardening as

$$d\sigma_i = C_{ij}^{EP}\, d\epsilon_j \tag{10}$$

where

$$C_{ij}^{EP} = C_{ij} - \frac{C_{ik}\frac{\partial f}{\partial \sigma_k}\frac{\partial f}{\partial \sigma_\ell} C_{\ell j}}{(C_{mn} + \beta_{mn})\frac{\partial f}{\partial \sigma_m}\frac{\partial f}{\partial \upsilon_n}} \tag{11}$$

The above equations have been implemented in a finite element program. In order to correlate the theory with existing test data, the material constants, a_{ij}, were estimated for EGCR-Type AGOT graphite.

Simple tension problems have been analyzed by the finite element program with both isotropic and kinematic hardening rules. As seen in Figure 4-14, the theory based on the kinematic hardening rule gives better correlation than that of the isotropic hardening rule. Additional comparison of the theory with experimental data is being carried out for a thick-walled cylinder.

B. Experimental Study on the Symmetric Modes of Vibration of a Four Bolt Clamped Rectangular Plate (H. Fenech, University of California at Santa Barbara)

The work reported is part of a research program initiated at the University of California, Santa Barbara, to assess the current design of the thermal barrier of the HTGR-PCRV (High Temperature Gas Cooled Reactor - Prestressed Concrete Reactor Vessel). Of particular

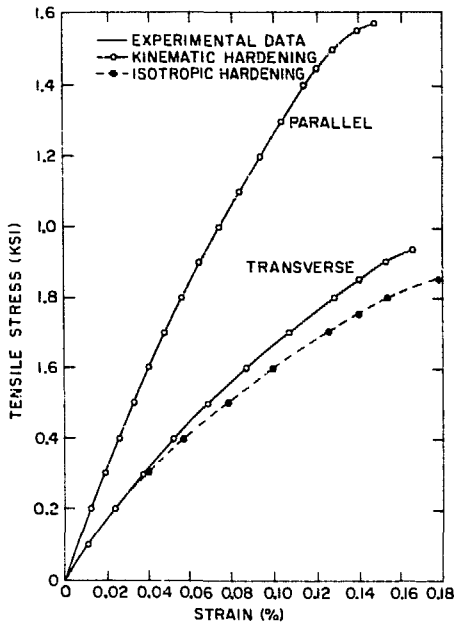

Figure 4-14. Comparison between elastic-plastic model and experiment data for AGOT-graphite.

interest is the response of the cover plate of the thermal barrier excited by the turbulent flow noise and the prediction of the fatigue lifetime of that cover plate. An earlier analysis[4-6] of the response of a square cover plate assumed that the natural modes of displacements and resonance frequencies were similar to those of a simply supported plate on all four sides. This assumption was motivated by the fact that a SS-SS-SS-SS plate (i.e., simply supported on all sides) is the only case which yields an analytic solution in the form of a product of two sine functions. The actual case of interest (i.e., a plate supported in the middle of the four sides by bolts) does not have a close form solution. A literature survey did not yield any data on the vibration of plates constrained by four bolts on the sides. It was thus decided to carry out a simple experimental program to obtain the missing data and identify the natural modes of vibration and their respective frequency.

Experimental Procedure

The tests were conducted on a 6061-T5 aluminum plate of 24" x 24" x 0.08". The plate was anchored in the middle of all four sides by 3/4" diameter bolts onto a 2" wooden board, leaving a gap of 5" between the plate and the board. The wooden board was solidly attached to a rigid angle iron frame.

The plate was excited by an electromagnetic excitor and the resonance frequencies were detected using a piezoelectric accelerometer (see Figure 4-15 showing the general arrangement of the experimental set up).

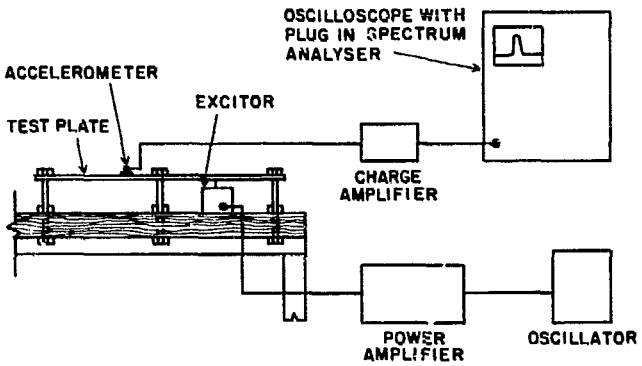

Figure 4-15. Test setup.

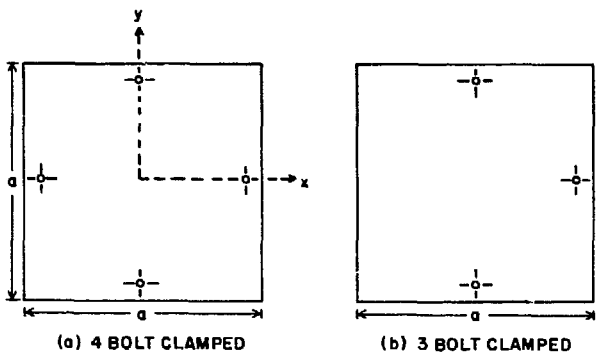

Figure 4-16. Test plate.

An EA-1250 "vibramate" excitor (M. B. Electronics) with the following performance characteristics was used in the tests:

Frequency range:	5-10,000 Hz
Force output:	0-25 lbs
Maximum displacement:	0.5"
Maximum velocity:	70"/sec
Maximum acceleration:	100 g
First resonance:	8900 cps

The power amplifier used to drive the excitor was an M. B. Electronics Model No. 2125, with the following specifications:

Power output:	125 v.a.
Frequency response:	5-20,000 Hz

The input signal source to the amplifier was provided by a wide range Hewlett-Packard oscillator Model No. 200 CD/CDR having the following specifications:

Frequency range:	5 Hz 600 KHz
Accuracy:	$\pm$2%
Output power:	160 milliwatts

The accelerator was a piezoelectric ENDEVCO-2215E having the following characteristics:

Frequency range:	20-20,000 Hz
Charge sensitivity:	173 pc/g
Capacitance:	10,500 pF
Transverse sensitivity:	2-3% maximum

The signal from the accelerometer was amplified by an amplifier Model No. 504 of Kistler Instruments and fed into a spectrum analyzer Model FSA-011 of Nelson Ross Electronics plugged in a Tektronix 535 oscilloscope. The above spectrum analyzer has a frequency range of 10 Hz - 20 KHz.

The mode shapes were formed by sprinkling household salt powder on the plate and recorded photographically on color prints. The cover plate was excited at different locations. In almost all cases an excitation point on or close to a model line gave the maximum displacement and clearer salt pattern. The stem of the excitor was clamped tightly to the plate to avoid unwanted noise.

Test Results

For the four bolt system (Figure 4-16a), the modes symmetric about the coordinate axis only, the modes symmetric about the diagonal axis only and the modes symmetric about both coordinate axis and diagonal axis were observed. Table 4-1 gives the resonance frequencies (Hz) and the corresponding dimensionless frequency parameter $(wa^2\sqrt{\rho/D}$, where w is the natural circular frequency, a the length of the plate edge, ρ the mass density per unit surface area of plate, and D the flexural rigidity of the three different sets). Because the sound waves generated by the turbulent eddies in the helium flow experience numerous scattering with the enclosing walls of the PCRV cavities, it is reasonable to assume that the exciting pressure on the cover plate is produced by plane wave with a direction of motion perpendicular to the plate. It is therefore expected that only the

TABLE 4-1

Experimentally Determined Frequency Parameters
for a Four Bolt Clamped Square Plate

Frequency cps	Frequency Parameter $wa^2\sqrt{\rho/D}$	Number of waves in x direction	Number of waves in y direction	±	Number of waves in y direction	Number of waves in x direction
Modes symmetric about coordinate axes only						
217.5	162.03	0	4	-	4	0
385	286.8	0	6	-	6	0
512	382	2	6	-	6	2
Modes symmetric about diagonals only						
41	30.5	1	1			
123.5	92	3	1	+	1	3
240.5	179.1	3	3			
363	270.4	5	1	+	1	5
444	330.7	5	3	+	3	5
659	490.9	7	1	+	1	7
789	587.8					
958	713.7	7	5	+	5	7
Modes symmetric about both coordinate axes and diagonals						
42.5	31.6	2	0	+	0	2
56.5	42.09	2	2			
104	77.4					
152	113.2	4	0	+	0	4
251	187.6	4	2	+	2	4
320	238.4					
387	288.3					
456	339.7	4	4			
475	356.2	6	0	+	0	6
485	363.7	6	2	+	2	6
593	444.8					
664	494.6					
782	582.5	6	4	+	4	6
861	641.4	8	0	+	0	8
930	692.8					
968	721.1	6	6			
981	730.8					
Modes antisymmetric about both coordinate axes and diagonals						
135	101.2	1	3	-	3	1
328	244.3	1	5	-	5	1
470	350.1	3	5	-	5	3
654	487.2	1	7	-	7	1
714	535.56	3	7	-	7	3
988	736	5	7	-	7	5

vibrational modes symmetric about both coordinate axis and diagonals will be excited.

It can be seen from Table 4-1, third entry on that table, that the natural modes of vibrations have a large number (17) of closely spaced resonance frequencies in the range 42.5-981 Hz. This is due to the large number of possible superposition of natural modes of different order in the x and y directions.

On Table 4-2 similar results are reported for a plate with only three bolts remaining. Because of the difficulty to identify the natural modes of displacement, the resonance frequencies and the dimensionless frequency parameters only are given in order of increasing frequencies. It is to be noticed that because of the reduced rigidity of the plate due to the loss of one bolt the first resonance frequency of 16.6 Hz is much lower than that of a four bolt plate (41 Hz). In the range 0-496.1 Hz forty-two separate resonance frequencies have been identified.

Although the dimensionless frequency parameter does depend on the Poisson's ratio in the general case when one or more edges are free, it is interesting to compare, for checking purposes, the fundamental dimensionless frequency parameter for square plates with different edge conditions. The results are given in Table 4-3 where seven different types of edge conditions are considered. The closest condition to the bolted plate is the one of a SS-SS-SS-SS plate with clamping at the side centers. As the ratio ℓ/a of clamping width to

TABLE 4-2

Experimentally Determined Frequency Parameters for a Three Bolt Clamped Square Plate

Mode	1	2	3	4	5	6	7
Resonant Frequency cps	16.6	30.5	40.1	47	69.5	118.5	150
Frequency Parameter $wa^2\sqrt{\rho/D}$	12.5	22.7	29.8	35	51.7	87.9	111.7

Mode	8	9	10	11	12	13	14
Resonant Frequency cps	179	185	213	234	245	286	293
Frequency Parameter $wa^2\sqrt{\rho/D}$	133.3	.36.3	158	174.3	182.5	213	218.2

Mode	15	16	17	18	19	20	21
Resonant Frequency cps	315	322	350	380	400	410	417
Frequency Parameter $wa^2\sqrt{\rho/D}$	234.6	239.8	260.7	283.1	298	305.4	310.6

Mode	22	23	24	25	26	27	28
Resonant Frequency cps	432	439	457	465	470	491	499
Frequency Parameter $wa^2\sqrt{\rho/D}$	321.8	327	340	346.4	350.1	365.7	371.9

Mode	29	30	31	32	33	-	34
Resonant Frequency cps	510	527	533	537	547	-	552
Frequency Parameter $wa^2\sqrt{\rho/D}$	379	392.6	397	400	407.5	-	411.2

Mode	35	36	37	38	39	40	41
Resonant Frequency cps	580	599	630	637.5	647	657	666
Frequency Parameter $wa^2\sqrt{\rho/D}$	432.1	446.2	469.3	474.5	482	489.4	496.1

TABLE 4-3

Fundamental Frequency Parameters* ($wa^2\sqrt{\rho/D}$) for Square Plates with Different Edge Conditions

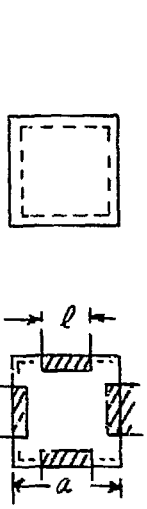

F F F F : - $wa^2\sqrt{\rho/D}$ = 14.14

SS SS SS SS : - $wa^2\sqrt{\rho/D}$ = 19.74

Clamped at four bolts ‡ : - $wa^2\sqrt{\rho/D}$ = 30.5

SS SS SS SS with Clamping at side centers : -

ℓ/a	0	1/3	1/2	1
$wa^2\sqrt{\rho/D}$	19.74	33.9	35.5	35.9

C C C C : - $wa^2\sqrt{\rho/D}$ = 35.9

C F F F : - $wa^2\sqrt{\rho/D}$ = 3.35

Clamped at three bolts ‡ : - $wa^2\sqrt{\rho/D}$ = 12.5

NOTE:

F : - Free edge

SS: - Simply supported edge

C : - Clamped edge

* Leissa: Vibration of Plates. Scientific Technical Information Division, NASA, 1969.

‡ From the present study.

total width increases from 0 to 1, the fundamental dimensionless parameter increases from 19.74 to 35.9.

The case of the cover plate with a dimensionless frequency parameter of 30.5 is between the ones with clamping ratios of 0 to 1/3 as expected. This parameter reduces to 12.5 when only three bolts remain in place. This value is lower than the one for a SS-SS-SS-SS plate ($\ell/a = 0$, $w^2 a \sqrt{\rho/D} = 19.74$). On the basis that the dimensionless frequency parameter, $wa^2\sqrt{\rho/D}$, is only dependent on geometry, the values obtained experimentally on an aluminum 6061-T6 plate, 24" x 24" x 0.08" were used to calculate the cyclic frequency of the plate cover of the FCRV insulation 42" x 42" x 0.375" using three different possible materials: carbon steel, Inconel-600, and Hastelloy X. The properties of those materials used for the calculations are given in Table 4-4. The results of the calculations are given in Tables 4-5 and 4-6. The size and thickness of the plate are the major contributors to the differences in cyclic frequencies between the experimental aluminum plate and the actual cover plate. The resonance cyclic frequencies of the actual cover plate for all three materials considered are close to each other with a fundamental mode frequency of 62.14 Hz for the carbon steel plate, 60.78 and 60.54 for the Inconel-600 and Hastelloy X plates, respectively.

Discussion of the Results

In the absence of an explicit analytical solution for the plate cover natural modes of vibrations, the most useful observation,

Table 4-4

Properties of Materials at $20^{\circ}C$ in the Present Work

Material	Weight density lb/in^3	E psi	Poisson's ratio
Al 6061-T6	.098	$10x10^6$	.33
Carbon Steel	.283	$29x10^6$	.3
Inconel 600	.304	$30x10^6$	.29
Hastelloy x	.297	$28.5x10^6$	.32

References

Handbook of Material Science Vol. II, CRC Press, 1974

Metals Handbook, American Society of Metals.

Metals Properties, ASME Handbook, 1954.

TABLE 4-5

Frequency Parameter $wa^2\sqrt{\rho/D}$ and corresponding resonant frequencies for 42"x42"x.375" (Four bolt clamped) plate of different materials.

$wa^2\sqrt{\rho/D}$	Resonant Frequencies in cps		
	Carbon Steel	Inconel 600	Hastelloy x
[illegible]			
[illegible]	52.1	50.8	50.5
[illegible]	64.4	63.0	62.7
83.1	85.8	83.9	83.6
77.4	157.7	154.2	153.6
92.9	187.4	183.3	182.6
101.2	206.3	201.7	200.9
113.2	230.6	225.6	224.7
162.0	330.1	322.9	321.6
179.1	364.9	356.9	355.5
187.6	382.2	373.9	372.4
238.4	485.7	475.1	473.2
244.3	497.7	486.9	485.0
270.4	550.9	538.9	536.8
286.8	584.3	571.6	569.3
288.3	587.4	574.5	572.3
330.7	673.7	659.0	656.5
339.7	692.1	677.0	674.3
350.1	713.3	697.7	695.0
363.7	741.0	724.8	722.0
382.0	778.3	761.3	758.3
444.8	906.2	886.4	883.0
487.2	992.6	970.9	967.1
490.9	1000.1	978.3	974.5
494.6	1007.7	985.7	981.8
535.5	1091.0	1067.2	1063.0
582.5	1186.8	1160.8	1156.3
587.8	1197.6	1171.4	1166.8
641.4	1306.8	1278.2	1273.2
692.8	1411.5	1380.7	1375.3
713.7	1454.1	1422.3	1416.8
721.1	1469.1	1437.1	1431.5
730.8	1488.9	1456.4	1450.7
736.0	1499.5	1466.8	1461.0

TABLE 4-6

Frequency Parameters $wa^2\sqrt{\rho/D}$ and corresponding resonant frequencies for 42"x42"x.375" (Three bolt clamped) plate of different materials.

$wa^2\sqrt{\rho/D}$	Resonant Frequencies in cps		
	Carbon Steel	Inconel 600	Hastelloy x
RUN			
12.5	25.5	24.9	24.8
22.7	46.2	45.2	45.1
29.8	60.7	59.4	59.2
35.0	71.3	69.8	69.5
51.7	105.3	103.0	102.6
87.9	179.1	175.2	174.5
111.7	227.6	222.6	221.7
133.3	271.6	265.6	264.6
136.3	277.7	271.6	270.6
158.0	321.9	314.9	313.6
174.3	355.1	347.4	346.0
182.5	371.8	363.7	362.3
213.0	434.3	424.5	422.8
218.2	444.5	434.8	433.1
234.6	478.0	467.5	465.7
239.8	488.6	477.9	476.0
260.7	531.1	519.5	517.5
283.1	576.8	564.2	562.0
298.0	607.1	593.9	591.6
305.4	622.2	608.6	606.2
310.6	632.8	619.0	616.6
321.8	655.6	641.3	638.8
327.0	666.2	651.7	649.1
340.0	692.7	677.6	674.9
346.6	706.1	690.7	688.0
350.1	713.3	697.7	695.0
365.7	745.1	728.8	726.0
371.9	757.7	741.1	738.3
379.0	772.2	755.3	752.4
392.6	799.9	782.4	779.4
397.0	808.8	791.2	788.1
400.0	814.9	797.1	794.0
407.5	830.2	812.1	808.9
411.2	837.8	819.5	816.3
432.1	880.3	861.1	857.8
446.2	909.1	889.2	885.8
469.3	956.1	935.3	931.6
474.5	966.7	945.6	941.9
482.0	982.0	960.6	956.8
489.4	997.1	975.3	971.5
496.1	1010.7	988.7	984.8

obtained from the present experimental work, is the similarity between the natural modes of vibration of a completely square plate and the one with a four bolt attachment at the middle of the side edges. The mode shapes for a free square plate are reproduced on Figure 4-17 from reference 4-7. For the present experiment with the bolted plate, each one of the photographs showing one natural mode have been arranged in a similar matrix of mode combinations. This arrangement is shown in Figure 4-18. The blank space in that figure belongs to natural modes which could not be excited by a "one-point" vibrator. The differences in the mode pattern occurs locally near the four bolts.

For the free plate, the displacement mode shapes can be approximated by the solution

$$W(x,y) = \cos\frac{m\pi x}{a}\cos\frac{n\pi y}{a} - \cos\frac{n\pi x}{a}\cos\frac{m\pi y}{a}.$$

The diagonal in the matrices of Figures 4-17 and 4-18 corresponds to the mode combinations with m = n. All the modes above the diagonal correspond to the combinations mn-nm and those below the diagonal to the combination mn + nm. It is therefore suggested that the analysis developed in reference 4-6 should be modified to incorporate the above approximate solution for the natural modes of displacement. In the case of a plane acoustical wave moving perpendicularly to the surface of the plate, only the modes symmetrical to both the xy and diagonal axis will be excited. Those modes have been identified in Table 4-1 and are represented by a combination of even values of m and n in the analytical expression.

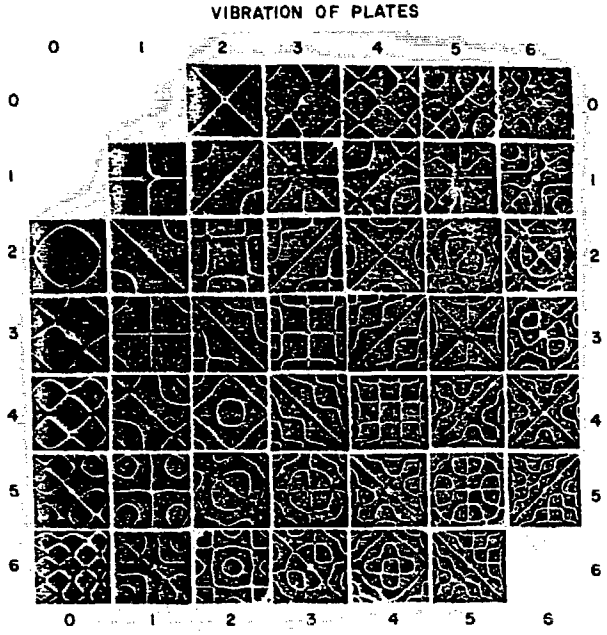

Figure 4-17. Experimentally determined mode shapes for a completely free square plate. (From ref. 4-7)

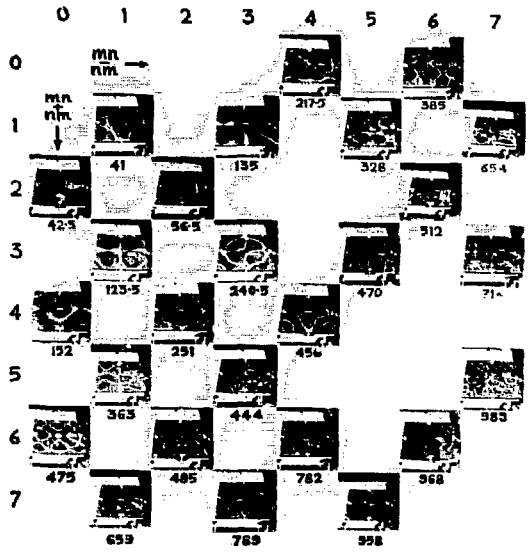

Figure 4-18. Experimentally determined mode shapes for a square plate bolted in the middle of the four edges (Cyclic frequencies in Hz).

References

4-1 OSCIL, BNL Horizontal Array Seismic Code, in press.

4-2 W. L. Greenstreet, "Constitutive Equations for Artificial Graphite," Ph.D. dissertation, Yale University, New Haven Connecticut, 1962.

4-3 W. L. Greenstreet, G. T. Yahr, and R. S. Valachovic, "The Behavior of Graphite Under Biaxial Tension," Carbon 11, 43-57 (1973).

4-4 T. Weng, "Stress-Strain Properties of Grade ATJ Graphite Under Combined Stresses," in Proceedings of the Conference on Continuum Aspects of Graphite Design, Gatlinburg, Tenn., Nov. 9-12, 1970. United States Atomic Energy Commission, CONF-701105, Feb. 1972.

4-5 R. M. Jones, D. A. R. Nelson, Jr., "A New Material Model for the Non-linear Biaxial Behavior of ATJ-S Graphite," J. Composite Materials 9, 10-27 (1975).

4-6 Henri Fenech, "An Analysis of Acoustic Flow Noise in Closed Systems and the Fatigue Lifetime of Structural Boundaries," Nucl. Eng. and Design, North Holland, in press, 1975.

4-7 Arthur W. Leissa, "Vibration of Plates," NASA-SP-160, p. 110, (1969).

V. Materials

A. Metal and Graphite Components (J. Chow, P. Soo)

During this reporting period a survey was conducted on equipment requirements to expand the capability of the mechanical testing laboratory. Amongst the most critical needs are a tensile machine for general testing, an additional fatigue machine, replacement control systems for an existing fatigue machine, and up to six creep machines. Several suppliers were contacted for negotiations and detailed hardware requirements have been established. Purchase orders will be placed when capital equipment funds are released.

Fatigue Testing of Incoloy 800

The high-cycle fatigue testing of Incoloy 800 continued. Several additional tests at 1200°F and 1400°F were completed and a complete summary of the test data is given in Figure 5-1. The data for 1400°F show that the fatigue endurance limit, if one exists, will be very low. Additional low-stress testing is required to evaluate this effect.

At 1200°F several tests were completed at alternating stress levels in the range 27,200-28,000 psi. Data are required in this regime since at slightly higher stress levels failure occurs rapidly and at slightly lower levels failure times are extremely long and usually necessitated termination of the test prior to fracture. However, the data in Figure 5-1 show that failure in this stress range still occurs in relatively short times and there is

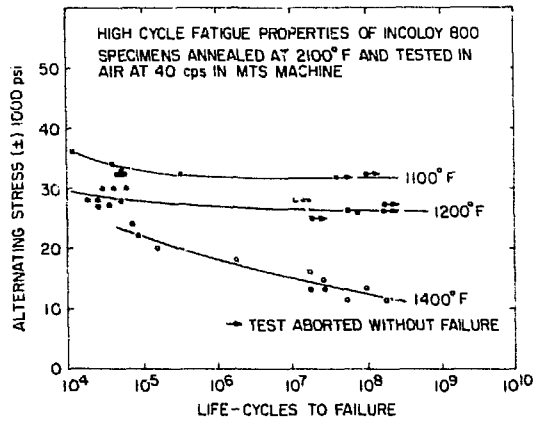

Figure 5-1.

little difference from the runs at 30,000 psi. It is clear that at 1200°F the fatigue life is extremely sensitive to the applied stress.

Work has continued on the commissioning of three stress-rupture machines which will be used for testing Incoloy 800. Furnaces and control equipment are being constructed and the equipment should be ready for use shortly.

B. Microstructure and Fracture of HTGR Graphites (J. E. Zimmer and R. A. Meyer -- The Aerospace Corporation)

The approach for this work is to determine the relation of microstructure to the mechanical and fracture behavior of HTGR graphites and the effect of various reactor environments on these relationships. At present crack propagation studies are being conducted on three possible candidate HTGR graphites: Union Carbide ATJ graphite used for structural support posts, Union Carbide PGX graphite used for the support blocks, and Great Lakes Carbon H451 moderator graphite. A wedge-opening, crack-propagation specimen is

stressed and observed in the scanning electron microscope. Controlled crack growth and direct observation of cracking and the graphite microstructure is made. Oxidation studies are being conducted on the ATJ and PGX graphites to determine how oxidization affects the graphite microstructure and fracture behavior. The use of an analytical model for the fracture of graphite to predict the properties of these graphites as a function of the reactor environments (e.g., oxidation) is being investigated.

Crack Propagation

Crack propagation studies on the ATJ and H451 graphites have assisted in identifying those microstructural features that affect fracture. With ATJ graphite the crack tends to follow microstructural discontinuities, producing the jagged appearance. Generally, cracking occurs by cleavage parallel to the graphitic basal layers. The crack path in ATJ graphite is dependent in part on the easy cleavage direction of the filler coke grains (average size - 70 μm) and on the relative orientation of these acicular grains to the crack direction. The H451 moderator graphite is a coarser grain graphite with the individual grains having an isotropic morphology. The crack path appears less jagged than that for the ATJ graphite. The deviations in the crack direction from a straight path occur on a scale similar to the 600 μm average grain size of the H451 graphite. Within a filler grain, the crack is relatively straight because the crack tends to follow the tightly folded graphitic layers characteristic of the fine isotropic morphology[5-1]. The crack deviations in this structure are very small (10-30 μm), compared to the larger deviations

(70-100 μm) due to the anisotropic needle coke grains in the ATJ graphite.

The crack propagation studies on the PCX graphite are in progress. Optical micrographs of this graphite (Figure 5-2) show its microstructure to consist of rather large needle coke grains (about 200 μm) with generally elongated pores.

Analytical Model

The analytical microstructural model for the fracture of graphite developed at Aerospace[5-2] predicts the tensile and compressive stress-strain and fracture behavior of bulk graphites based on microstructural parameters. These parameters include grain and pore size, porosity, grain cleavage strength, anisotropy, zero-porosity modulus, and fracture toughness. The model has been modified to include three grain/pore sizes. This permits modeling a graphite as having two fixed grain and pore sizes and one variable size. Thus, oxidation of graphite could be modeled as an increase in the size of certain accessible pores.

For the application of this fracture model to ATJ graphite, its microstructure was modeled as consisting of an average grain size of 70 μm with 10 v/o 200 μm grains, and 22% porosity (70% 70 μm pores, 30% 200 μm pores). These parameters are inserted into the associated computer code and the stress-strain curves in the against-grain direction were predicted and are shown in Figure 5-3. The predicted values of fracture stress in tension and compression (3.64 and 9.00 ksi) agree well with the manufacturer's values (3.40 and 8.80 ksi).

Figure 5-2. Optical micrograph of PGX graphite.

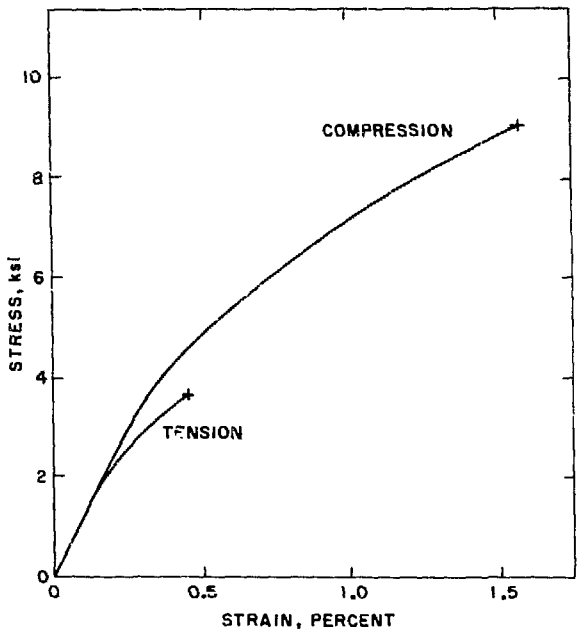

Figure 5-3. Predicted stress-strain curves in tension and compression in the against-grain direction for ATJ graphite.

To illustrate the applicability of the analytical model to predicting the effects of reactor environment, for example, oxidation due to water in the helium coolant, the fracture stress of ATJ graphite has been predicted as a function of the porosity. The effect of oxidation on the fracture of ATJ graphite may be selective removal of material from certain accessible pores. (The microstructural details of this oxidation will be studied during this program.) Modeling this effect involved increasing the size of 20% of the 70 μm pores to allow for an increase in the bulk porosity. The fracture stress of ATJ graphite in tension and compression as a function of porosity is shown in Figures 5-4 and 5-5. In compression, a 10% increase in porosity due to oxidation results in about an 11% reduction in fracture stress. These figures represent only a demonstration of how this analytical model might be applied to predicting reactor graphite properties as a function of environment. The actual details of the microstructural changes due to oxidation and quantitative data such as percent burn-off per year need to be obtained from this and other programs.

Oxidation

A furnace and associated controls for oxidation studies have been set up and are operational. Specimens will be oxidized in dry air for 1 hour at 400, 500, 600 and 700°C. These specimens will be observed by optical and scanning electron microscopy to determine the changes in microstructure due to this oxidation.

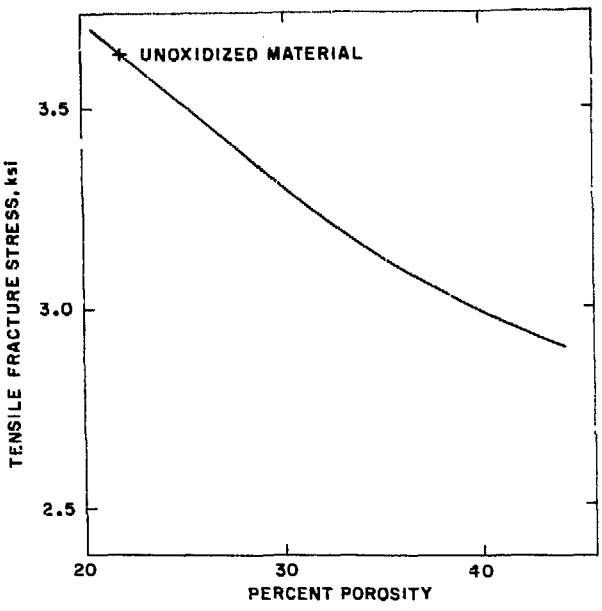

Figure 5-4. Effect of increase in porosity due to oxidation on the against-grain tensile fracture stress of ATJ graphite, as predicted by the analytical fracture model.

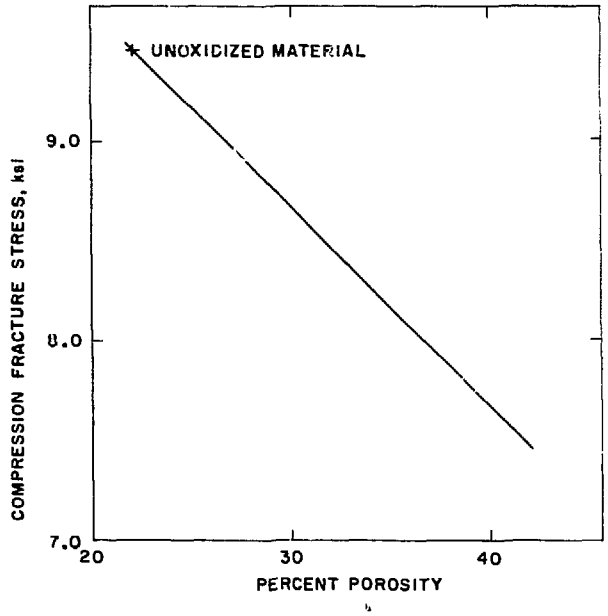

Figure 5-5. Effect of increase in porosity due to oxidation on the against-grain compressive fracture stress of ATJ graphite, as predicted by the analytical fracture model.

The crack propagation studies on PGX graphite will be completed. Oxidation of both the ATJ and PGX graphites will be studied. The changes in microstructure as a result of oxidation may be different for these two graphites, thus identification of the modes of fracture and fracture strength (as predicted by the analytical model) pre- and post-oxidation should provide valuable information about their structural integrity.

C. Materials Data Base (S. Nicolosi)

A literature search is being performed to collect the physical and mechanical properties data of candidate HTGR materials. The data to be used for some alloys (i.e., 2¼Cr 1Mo, 316 S.S., Inconel 718) have previously been collected and evaluated for the Nuclear Systems Materials Handbook (TID-26666) being prepared by the Hanford Engineering Development Laboratory for ERDA.

The primary effort has been directed towards collecting data pertaining to the physical and mechanical properties of graphites including candidate HTGR graphites. The graphite types under consideration are Great Lakes Carbon's H451, H327, H440, H359 and HLM; Pure Carbon's P03, Stack Pole 2020 and Union Carbide's PGX and ATJ. Of these, relatively extensive data appear readily available only for ATJ. Thus far, manufacturers data have been received on PGX, HLM and 2020 graphites.

D. Compilation and Assessment of Properties of Concrete for Use in Establishing Criteria for PCRV Safety Analysis

(A. Auskern and L. E. Kukacka)

In past progress reports[5-1 to 5-3,5-4] reference has been made to the large volume of published work concerned with the properties of concrete as it relates to pressurized concrete reactor vessels. This concrete is concrete in the conventional sense, that is, it consists of coarse and fine aggregate mixed with cement and water and then cast into place. All the tests and properties that have been reported were measured on concretes of this type. However, a significant volume of the Fort St. Vrain pressure vessel contains concrete prepared by the preplaced aggregate technique (PAC)[5-5,5-6]. This is a procedure used for placing concrete in areas where there are severe space interference problems and difficult accesses. In this procedure the coarse aggregate is first placed by hand and rodded, then a fluid grout is pumped into the interstices between the coarse aggregate particles and allowed to harden, forming the concrete. In the Fort St. Vrain PCRV, preplaced aggregate concrete is used for the bottom head liner and core support floor. It is estimated that about 40% of the concrete (based on model 2) consists of preplaced aggregate concrete[5-5]. Limited surveys of other PCRV's indicate that PAC is not widely used[5-7]. Concrete prepared in this manner is discussed in "Concrete for Nuclear Reactors" in connection with relatively low strength concrete used for shielding purposes[5-8]. The placing procedure is also discussed in the 1964 ORNL state-of-the-art report

on concrete for PCRV's[5-9].

Because of a general lack of extensive research on PAC as applied to PCRV, and because of its use in a major portion of at least one PCRV, a literature survey has been undertaken in an attempt to evaluate this material regarding its long term applicability to PCRV's. The most obvious question one would have concerning PAC is the ability to fill with grout all the interstices within the packed aggregate. Much of the development work on PAC is of course directed towards this end. The mix design for PAC differs from that of a normally placed concrete in that it contains considerably more coarse aggregate (~57% as compared to 30% by volume for the Fort St. Vrain reactor vessel model 2, for example)[5-5]. The mortar, or grout is designed to be much more fluid than a conventional mortar, so that it may be pumped into the placed large aggregate. Sometimes fly ash and special additives are used to aid in the mobility of the grout and retard its set. However, problems with incomplete penetration can occur[5-5], especially in particularly congested areas. Repairs to incompletely penetrated areas can be made using a dry pack concrete. The real problem may be in locating void areas within the concrete mass. One of the standard grout ingredients is a fluidifier which aids in the mobility of the grout by generating hydrogen gas in the grout mix before the initial set. It is felt that the hydrogen gas will not embrittle the exposed steel[5-6].

It is obvious that the internal structure of PAC differs considerably from that of conventionally placed concrete. In PAC, the coarse aggregate pieces are in tight contact with each other in three dimensions, while in normal concrete the large aggregate particles are each surrounded by mortar. This difference can result in different mechanisms of stress transfer through the concrete, and in a different fracture mechanism. It has been observed for PAC used for shielding, that the stress-strain curve differs in shape from that of conventionally placed concrete[5-8]. The compressive strength of PAC specimens appears similar to that of the regular concrete, although it is not clear from the discussions exactly how the samples were prepared[5-5,5-6]. It is assumed that for test specimens of PAC, the aggregate is first packed into the mold and then the grout poured in. There are indications that PAC suffers a greater reduction in strength with temperature than conventionally placed concrete[5-8], but there appears to be little information on the temperature dependence of PAC vis-a-vis pressure vessel application. The properties of PAC are reported to be identical with those of conventional concrete used in the Fort St. Vrain model 2[5-5].

The effort on evaluating preplaced aggregate concrete will continue with the acquisition of additional pertinent documents.

References

5-1 HTGR Safety Evaluation Division Quarterly Report, April-June 1975, BNL-50460.

5-2 J. D. Buch, J. E. Zimmer, R. A. Meyer, ATR-74(7425)-4. The Aerospace Corporation, June 1974.

5-3 Summary Report, HTGR Safety Evaluation Division, BNL-19763, February 1975.

5-4 HTGR Safety Evaluation Division Quarterly Report, January-March 1975, BNL-50450.

5-5 Prestressed Concrete Reactor Vessel Model 2, GA-7150, General Atomics Division, General Dynamics Corporation, San Diego, California, 1966.

5-6 Final Safety Analysis Report, Fort St. Vrain Nuclear Generating Station, Vol. II, Section 5.4.

5-7 Chen Pang Tan, "Prestressed Concrete in Nuclear Pressure Vessels: A Critical Review of Current Literature," ORNL-4227, May 1968.

5-8 H. S. Davis, "N-Reactor Shielding," paper SP34-52 in Concrete for Nuclear Reactors, p. 1109, Vol. II, SP-34, Amer. Concrete Inst., Detroit, 1972.

5-9 State of the Art of Prestressed Concrete Pressure Vessels for Nuclear Power Reactors, A Critical Review of the Literature, ORNL-TM-812, June 1964.

VI. Instrumentation and Monitoring (A. Romano)

Specifications for the gas chromatograph to be purchased for use on the HIL test loop were rewritten to include automatic peak area integration. This will allow the device to be used for quantitative measurements of the H_2, O_2, N_2, CH_4, CO, CO_2 and H_2O levels of the loop over a range of from 10-1000 ppmv.

Specifications for the mass spectrometer system (to be used at Fort St. Vrain) have been rewritten to include a gas chromatograph with a He ionization detector in addition to the mass spectrometer. The integrated instrument will have the capability of monitoring H_2, H_2O, N_2, O_2, CO, CH_4 and CO_2, as well as fission products such as tritium, Xe, Kr, etc.

The specifications were rewritten to achieve a sensitivity of 1 ppbv for fission product gases and 1 ppmv for the other impurity gases.

Both requisitions have had bids solicited and received. An evaluation of the bids is presently under way.

IX. Phenomena Modeling and Systems Analysis

A. HTGR Safety Code Library (J. Beerman)

During the reporting period conversion to the CDC 7600 system of the codes SORSD and GAKIT was completed and conversion of the codes CORCON and RECA continued. Work on RECA was suspended in April 1975 due to inconsistencies between input data and output results and lack of one module of the program. A complete new set of input data, sample output and updated program was received in July and the conversion effort was resumed. The General Atomic Company proprietary code TAP was received and conversion work initiated.

Copies of the GA proprietary code TAP (unconverted) were sent to John Sanders at Oak Ridge National Laboratory and to William Kirk at Los Alamos Scientific Laboratory and the proprietary code OXIDE-3 was also sent to Oak Ridge.

Table 9-1 summarizes the status of the 29 programs currently being maintained in the library.

B. OXIDE-3 (J. Skalyo, Jr.)

The OXIDE-3 code has been used to calculate the equilibrium impurity concentrations in the primary coolant stream for different values of the effective diffusion constant Z, where

$$Z = \left(\frac{\varepsilon}{q}\right) D.$$

The porosity-tortuosity factor $\frac{\varepsilon}{q}$ is a property of the type of graphite

Table 9-1

HTGR Safety Code Library

Program	Status	Proprietary	Function
CRECT	OP	NP	Corrects data on ENDF/B tape.
LISTFC	OP	NP	Lists data from ENDF/B tape.
RIGEL	OP	NP	Manipulates data on ENDF/B tape.
ENDFB2	OP	NP	Converts data on ENDF/B tape to binary.
FLANGE	OP	NP	Prepares thermal cross section transfer arrays.
GAND2	OP	NP	Prepares fine group fast, resonance, and thermal cross sections from ENDFB2 binary tapes.
GFE2	OP	NP	Prepares fine group fast cross sections from ENDFB2 binary tapes.
MAKE	OP	NP	Prepares fine group fast cross section tape from GFE2 for spectrum codes.
WTFG	OP	NP	Prepares fine group thermal cross section tape from GAND2 or FLANGE for spectrum codes.
PRINT	OP	NP	Reads the fast cross section tape produced by MAKE.
SPRINT	OP	NP	Reads the thermal cross section tape produced by WTFG.
GGC4	OP	NP	Prepares broad group cross sections from MAKE and WTFG tapes.

C = In the process of being converted to the CDC-7600.
OP = Operational on the BNL CDC-7600 system under Scope 2.
R = Recently received from General Atomic Co. or Argonne Code Center.
P = General Atomic Company proprietary code.
NP = Not considered to be a proprietary code.

Table 9-1 Cont'd.

Program	Status	Proprietary	Function
INTERP	OP	NP	Prepares broad group cross sections from MICROX output data tapes.
IDX	OP	NP	Performs one-dimensional, diffusion theory, steady-state calculations.
FEVER-7	OP	NP	Performs one-dimensional, diffusion theory, burnup and reload calculations.
TEMCO-7	OP	NP	Computes reactor temperature coefficients from input cross section data.
BLOOST-7	OP	NP	Performs zero-dimensional reactor kinetics calculations.
GAKIT	OP	NP	Performs one-dimensional reactor kinetics calculations.
TWIGL	OP	NP	Performs two-dimensional light-water reactor kinetics calculations.
TAC-2D	OP	NP	Performs two-dimensional, transient conduction analyses.
FLAC	OP	NP	Calculates steady-state flow distributions in arbitrary networks with heat addition.
POKE	OP	P	Calculates steady-state flow distribution and fuel and coolant temperatures in a gas-cooled reactor.
RECA	C	P	Calculates time-dependent flow distribution and fuel and coolant temperatures in the primary system.
CORCON	C	P	Computes the temperature history and fission product redistribution following a loss of all convective cooling of the core.

Table 9-1 Cont'd.

Program	Status	Proprietary	Function
SORS	OP	P	Computes the release of volatile and non-gaseous fission products from an HTGR core during thermal transients.
GOPTWO	OP	NP	Analyzes the steady state graphite burnoff and the primary circuit levels of impurities.
OXIDE-3	OP	P	Analyzes the transient response of the HTGR fuel and moderator to an oxidizing environment.
SAMPLE	OP	NP	Propagates uncertainties in probability distributions by Monte Carlo technique.
TAP	C	P	Calculates the transient behavior of the integrated HTGR power plant.

and D is the free gas diffusion constant of the impurity gas in helium. In this study $\frac{\varepsilon}{q}$ was varied from 10^{-3} to 10^{-2} (GA-LTR-7 suggests 10^{-2}) and the impurity concentrations were obtained for a 3000 MW(th) HTGR operating at full power with a fixed steam leak of 0.09 lb/h (this leak gives a combined CO, H_2O impurity concentration of 10 ppmv).

The calculation assumes most of the same input as does the sample problem shown in Section 9 of GA-LTR-7 (a transient with steam tube rupture). Here, however, the reactor was not scrammed and a step function steam leak rate is started at t=0. The time dependence of the impurity partial pressures was then calculated over the range $0 < t < 200$ ksec. Equilibrium values P_o were then obtained by fitting the equation

$$P = P_o - P_1 \exp(-\lambda_1 t) - P_2 \exp(-\lambda_2 t)$$

to the time dependent OXIDE-3 results by the method of least squares. An excellent fit was obtained to the computer generated data; a phenomenological justification of the fitted equation was given in the previous progress report[9-1].

The results of the OXIDE-3 calculations for three values of $\frac{\varepsilon}{q}$ are shown in Figures 9-1 to 9-4 for steam, hydrogen, carbon monoxide, and the CO/H_2O ratio, respectively; the parameters of the least squares calculations are given in Table 9-2. An indication of whether there is substantial fuel hydrolysis can be obtained by

using the conservation relation

$$L = K_1 \ (C_{St} + C_{CO}).$$

For a steam leak L rate of 0.005 moles per hour and a purification factor K_1 of 10% per hour, the primary impurity inventory of $C_{St} + C_{CO}$ is 0.05 moles. Transforming this to the equivalent in terms of partial pressure, with a helium inventory of 4991 moles and a total pressure of 718.2 psia, the result is $P_{St} + P_{CO} = 7.19$ mpsia. The calculated values are 7.16, 7.07, and 7.02 mpsia for $\frac{\epsilon}{q}$ equal to 10^{-3}, 5×10^{-3}, and 10^{-2}, respectively, showing an increasing discrepancy with larger diffusion coefficient. The amount of fuel hydrolysis increases as Z increases, as expected; however, the magnitude indicated is believed to be in error due to a coding mistake discussed later.

The sensitivity of the impurity concentrations to a variation in the steam-graphite reaction rate has been illustrated[9-1]. The Langmuir-Hirshelwood equation for the reaction rate (Eq. 3-33 of GA-LTR-7) has been multiplied by a factor F with values 100, 1, and 0.01; again the steam leak rate is 0.09 lb/h. The least squares analysis has been completed and the results are given in Table 9-3. The values for $P_{St} + P_{CO}$ are 5.27, 7.02, and 7.24 mpsia for F equal to 0.01, 1.0, and 100.0 respectively; substantial hydrolysis of fuel is encountered when F = 0.01 (again it is believed that a correction of an OXIDE-3 coding error would reduce this hydrolysis).

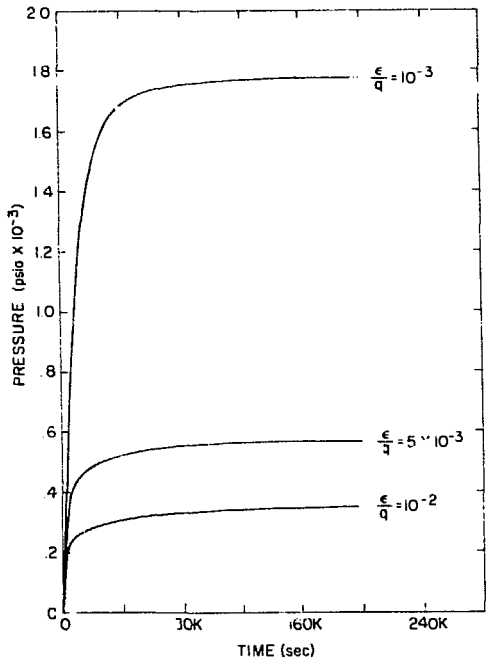

Figure 9-1. Partial pressure of steam in the hot plenum as a function of time due to a step function leak rate L = 0.09 lb/h for various gas-graphite diffusion factors ϵ/q.

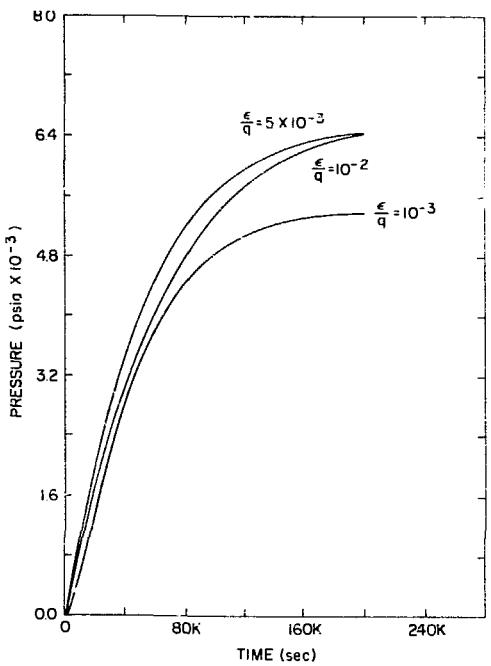

Figure 9-2. Partial pressure of hydrogen in the hot plenum as per Figure 9-1.

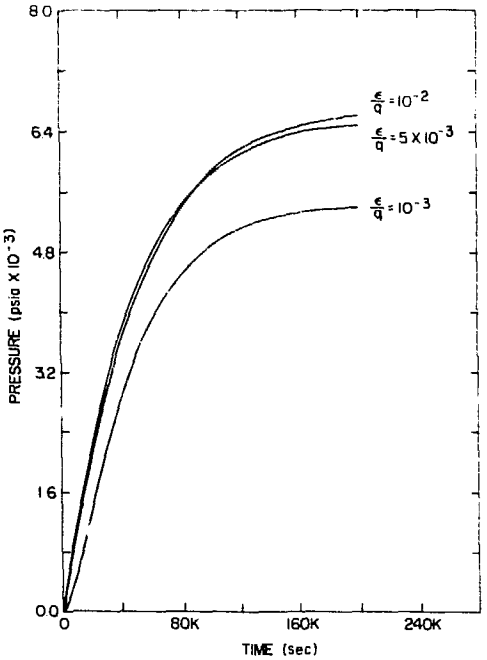

Figure 9-3. Partial pressure of carbon monoxide in the hot plenum as per Figure 9-1.

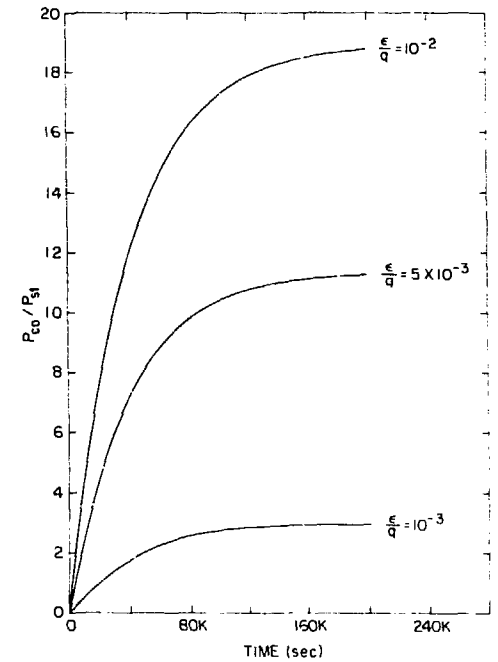

Figure 9-4. The ratio of the partial pressures of carbon monoxide and steam in the hot plenum as per Figure 9-1.

Table 9-2

$\frac{\varepsilon}{q}$ Variation (P_i in mpsia and λ_i in sec^{-1})

Impurity	P_o	P_1	λ_1	P_2	λ_2
		A. $\frac{\varepsilon}{q} = 10^{-3}$			
Steam	1.77	1.46	1.2×10^{-4}	0.31	3.3×10^{-5}
Hydrogen	5.39	-1.43	1.2×10^{-4}	6.82	2.5×10^{-5}
Carbon Monoxide	5.39	-1.50	1.2×10^{-4}	6.89	2.6×10^{-5}
		B. $\frac{\varepsilon}{q} = 5\times10^{-3}$			
Steam	0.569	0.408	4.1×10^{-4}	0.157	2.9×10^{-5}
Hydrogen	6.50	-0.32	3.3×10^{-4}	6.83	2.1×10^{-5}
Carbon Monoxide	6.50	-0.39	3.4×10^{-4}	6.90	2.3×10^{-5}
		C. $\frac{\varepsilon}{q} = 10^{-2}$			
Steam	0.349	0.228	7.0×10^{-4}	0.117	2.5×10^{-5}
Hydrogen	6.68	-0.07	1.4×10^{-3}	6.75	1.6×10^{-5}
Carbon Monoxide	6.67	-0.17	5.2×10^{-4}	6.85	2.1×10^{-5}

The results of varying the leak rate ($\frac{\varepsilon}{q}$ and F are the nominal OXIDE-3 values of 10^{-2} and 1.0 respectively) were also illustrated[9-1]. The least squares analysis of these calculations are given in Table 9-4 for leak rates 0.009, 0.09, and 0.9 lb/h; the values for $P_{St} + P_{CO}$ are 0.710, 7.02, and 69.0 mpsia respectively.

Evidence of fuel hydrolysis is found for all of the parameter studies and is a large effect for the case in which F = 0.01, at least. For the case with L = 0.09 lb/h, F = 1.0, and $\frac{\varepsilon}{q} = 10^{-2}$, the rate of fuel hydrolysis at t = 200 ksec (a point thought to be near equilibrium) is 6.8×10^{-10} core fraction per second. This amounts to 2% hydrolysis per year; but it is clear that some elements are higher than the core averages since a preferential steam-fuel reaction is occurring in the cooler fuel elements where the graphite web is not sufficiently hot to getter the steam. At L = 0.9 lb/h one obtains 31% hydrolysis per year.

The steam-fuel reaction rate is insensitive to temperature compared with the steam graphite reaction rate. Since the reactor purification time constant is 10 hours, it is worthwhile investigating the fuel hydrolysis that occurs during an accidental steam leak with reactor scram. The reduction in core temperature would eliminate the steam-graphite gettering process while supplying substantial water for fuel hydrolysis for an extended time.

For this illustration, the example of GA-LTR-7 in Section 9 has been extended to 200 ksec. The long time behavior for

Table 9-3

F Variation (P_i in mpsia and λ_i in sec^{-1})

Impurity	P_o	P_1	λ_1	P_2	λ_2
		A. F = 0.01			
Steam	1.17	0.66	1.9×10^{-4}	0.49	3.3×10^{-5}
Hydrogen	4.07	-0.29	1.7×10^{-4}	4.37	1.9×10^{-5}
Carbon Monoxide	4.10	-0.51	1.5×10^{-4}	4.62	2.4×10^{-5}
		B. F = 1.0			
Steam	0.349	0.228	7.0×10^{-4}	0.117	2.5×10^{-5}
Hydrogen	6.68	-0.07	1.4×10^{-3}	6.75	1.6×10^{-5}
Carbon Monoxide	6.67	-0.17	5.2×10^{-4}	6.85	2.1×10^{-5}
		C. F = 100.0			
Steam	0.190	0.170	1.1×10^{-3}	0.019	3.2×10^{-5}
Hydrogen	7.05	-0.04	4.5×10^{-3}	7.09	1.6×10^{-5}
Carbon Monoxide	7.05	-0.12	8.9×10^{-4}	7.17	2.0×10^{-5}

Table 9-4

L Variation (P_i in mpsia and λ_i in sec^{-1})

Impurity	P_o	P_1	λ_1	P_2	λ_2
		A. L = 0.009 lb/h			
Steam	0.0249	0.0200	8.6×10^{-4}	0.0047	2.6×10^{-5}
Hydrogen	0.685	-0.005	3.7×10^{-3}	0.690	1.6×10^{-5}
Carbon Monoxide	0.685	-0.013	8.2×10^{-4}	0.699	2.1×10^{-5}
		B. L = 0.09 lb/h			
Steam	0.349	0.228	7.0×10^{-4}	0.117	2.5×10^{-5}
Hydrogen	6.68	-0.07	1.4×10^{-3}	6.75	1.6×10^{-5}
Carbon Monoxide	6.67	-0.17	5.2×10^{-4}	6.85	2.1×10^{-5}
		C. L = 0.9 lb/h			
Steam	5.78	2.93	4.6×10^{-4}	2.76	2.7×10^{-5}
Hydrogen	63.1	-1.4	1.8×10^{-4}	64.7	1.6×10^{-5}
Carbon Monoxide	63.2	-2.5	2.9×10^{-4}	65.8	2.1×10^{-5}

the steam, hydrogen, and carbon monoxide are shown in Figures 9-5 to 9-7, respectively; some structure in the curves at times 0-2 ksec is observed. The results are as expected in that the purification system eventually cleans the primary coolant stream. The steam-graphite reaction is small after 10 ksec due to the scram. The fraction of UC_2 hydrolyzed is shown in Figure 9-8 and gives ≈30% as an equilibrium value.

This latter result is apparently due to a coding error since the average failed fuel fraction in the core is only 1.58%. Investigation of the code indicates that all the UC_2 in the fuel element is permitted to react with the steam and a clarification has been sought from G.A. on this point. It would appear that hydrolysis effects in the code are on the average 60 times too high.

Finally, we have compared the noble gas release with a similar calculation appearing in GA-A13171. Reasonable agreement is attained during the time scale 0-1.4 ksec (the length of time depicted in Figure 5-10 of GA-A13171). This calculation does appear to be correct in the coding as only failed fuel is allowed to give off noble gas contamination. We do <u>not</u> however agree with statements in GA-A13171 that the release is leveling off after 1.4 ksec at a value of ~100 kCi. At 200 ksec our results show a release of 3.3 MCi; this number is in agreement with the point that a major portion of the failed fuel is hydrolyzed and its noble gas inventory released before the purification system can clean the primary of steam.

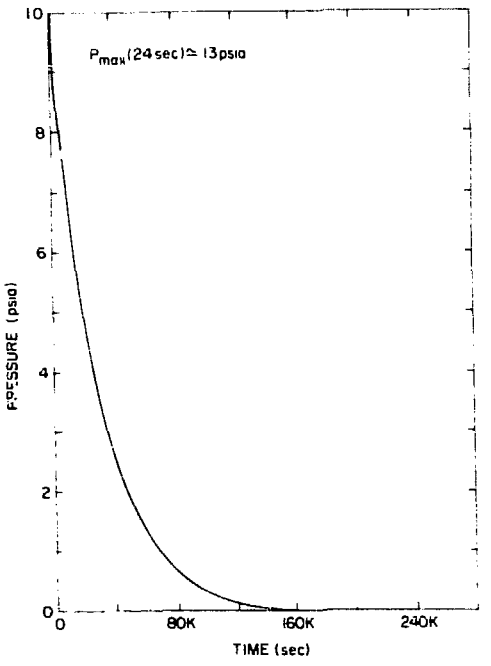

Figure 9-5. Partial pressure of steam in the hot plenum as a function of time due to a transient 1526 lb steam leak and resultant scram.

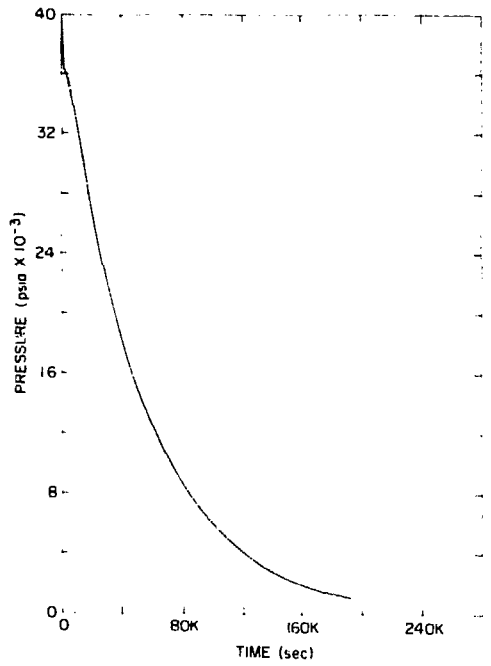

Figure 9-6. Partial pressure of hydrogen in the hot plenum as per Figure 9-5.

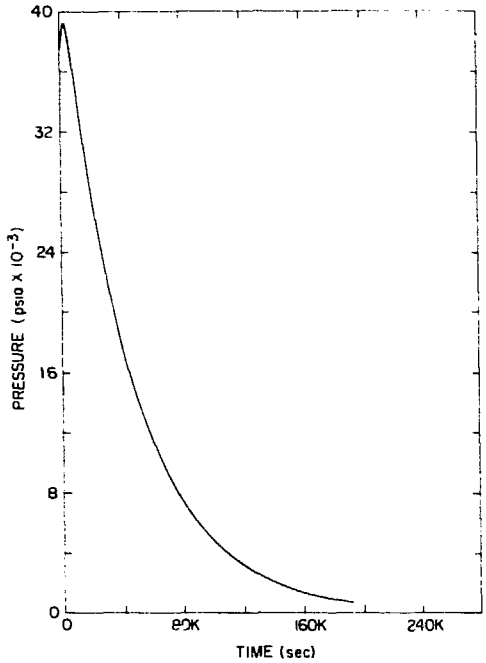

Figure 9-7. Partial pressure of carbon monoxide in the hot plenum as per Figure 9-5.

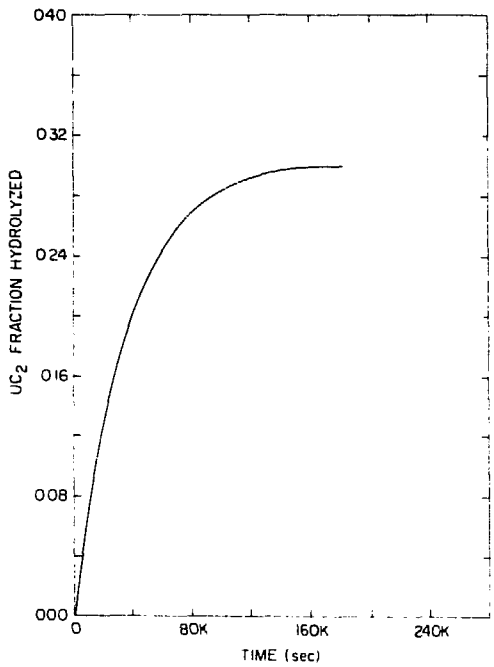

Figure 9-8. Fraction of UC_2 fuel inventory hydrolyzed as per Figure 9-5.

C. Comparison of GOPTWO and OXIDE-3 Parametric Study (L. Epel)

Although there are many basic differences in the intent and uses of the GOPTWO code vis-a-vis the OXIDE-3 code, there is also a common area in which the two codes can be applied. Such a regime has already been investigated using OXIDE-3[9-1], and now GOPTWO has been exercised to cover the same regime. The purpose of this study was twofold: it offers an opportunity to verify both codes, in a rather gross way, in order to ascertain if, at least in their area of commonality, any blunders have been programmed into either of them and at the same time it yields a general picture of which variables are important and which are more or less incidental to the final results.

The input to the two codes was made as internally consistent as the input formats allow. Where the modeling in the two codes is so different that completely different data are called for, every attempt was made to make the input compatible between the two. Even so, it was impossible to guarantee that each code was run precisely under the same conditions or with exactly the same geometry and values of variables. From an engineering point of view, however, the two codes were made to solve a very similar set of problems.

The problems addressed in these runs concern steady-state operation at full reactor power and they focus on the graphite-water reaction, assuming a constant water ingress rate. A set of "nominal" conditions were specified and three important input parameters were varied from these conditions. Since the graphite-water

reaction yields hydrogen and carbon monoxide in equal amounts, attention was directed to the steady-state concentrations of water vapor and carbon monoxide exclusively.

The parameters that were varied were:

1) graphite-water reaction rate (R)

2) diffusion coefficient of water vapor in graphite (D)

3) water ingress rate into system (L).

The "nominal" values of these were taken to be, respectively:

$$R(\%/h) = \frac{1069 \times 10^{7} \exp(-40900/\bar{R}T)\, P_{H_2O}}{1 + 0.0166 \exp(28600/\bar{R}T) P_{H_2}^{0.75} + 0.0531 \exp(27500/\bar{R}T)\, P_{H_2O}}$$

where the partial pressures are given in atmospheres,

$$D\ (cm^2/sec) = 1.00 \times 10^{-6} \frac{T^{1.58}}{P_{total}}$$

where the temperature is in degrees Kelvin and the total pressure is in atmospheres, and L = 0.09 lb/h (which is the ingress rate that yields 10 ppm of oxidants in the coolant stream with the above conditions).

The comparison of the two codes was done with the reaction rate two orders of magnitude larger and then two orders of magnitude smaller than the nominal value. The the diffusion coefficient and water ingress rates were each separately varied by an order of magnitude above and below the nominal values. The results of the seven separate cases thus obtained are summarized in Tables 9-5 and 9-6.

Table 9-5

Comparison of GOPTWO and OXIDE-3 Results
Steady-State Water Concentration (psia)

k	D	L	GOPTWO	OXIDE-3	% Difference
1	1	0.1	2.64 E-5	2.49 E-5	6
1	1	1	5.34 E-4	3.49 E-4	35
1	1	10	1.10 E-2	5.78 E-3	47
1	0.1	1	1.45 E-3	1.77 E-3	-22
1	1	1	5.34 E-4	3.49 E-4	35
1	10	1	1.74 E-4	5.43 E-5	69
0.01	1	1	3.18 E-3	1.17 E-3	63
1	1	1	5.34 E-4	3.49 E-4	35
100	1	1	*	1.90 E-4	*

*The GOPTWO code becomes unstable for certain combinations of reaction rate, diffusion coefficient, water ingress rate and initial estimates of impurity concentration.

Table 9-6

Comparison of GOPTWO and OXIDE-3 Results
Steady-State Carbon Monoxide Concentration (psia)

k	D	L	GOPTWO	OXIDE-3	% Difference
1	1	0.1	6.97 E-4	6.85 E-4	1.7
1	1	1	6.70 E-3	6.67 E-3	0.4
1	1	10	6.13 E-2	6.32 E-2	3.1
1	0.1	1	5.78 E-3	5.39 E-3	6.7
1	1	1	6.70 E-3	6.67 E-3	0.4
1	10	1	7.06 E-3	6.83 E-3	3.3
0.01	1	1	4.05 E-3	4.10 E-3	1.2
1	1	1	6.70 E-3	6.67 E-3	0.4
100	1	1	*	7.05 E-3	*

*The GOPTWO code becomes unstable for certain combinations of reaction rate, diffusion coefficient, water ingress rate and initial estimates of impurity concentration.

The nominal case resulted in good agreement (35% difference in water vapor concentration and ~1/2% difference in carbon monoxide concentration) between the two codes. It was found that the concentration of helium impurities that GOPTWO computes is strongly influenced by the temperature profile that is input to the code. Although care was taken to make this data consistent with similar input to OXIDE-3, absolute compatibility could not be achieved (due to differences in modeling and input requirements between the two codes). The 35% discrepancy is believed to represent essential agreement between the two codes at nominal conditions. The largest disagreement between the two codes came about when either the graphite-water reaction rate was low or the diffusion rate of water in graphite was high. In both of these situations it is easier for the water vapor to diffuse through the graphite web to reach the fuel stick. Notice that in both of these situations the free-steam concentration of water vapor computed by OXIDE-3 was lower than that computed by GOPTWO. Since it was not feasible to "shut off" the fuel hydrolysis reaction while running OXIDE-3, and since this reaction is not considered in GOPTWO, such a discrepancy is not unexpected. Indeed, some analysis on the OXIDE-3 results has been done that substantiates the thesis that part of the discrepancy in results between the two codes is due to this fuel hydrolysis reaction.

The second objective in running this parametric study, viz. to obtain an appreciation of the effect of the salient variables in GOPTWO, was accomplished by extending the survey beyond the regime

used to compare results with those of OXIDE-3. By holding the graphite-water reaction rate constant at the nominal value, the effect of diffusion coefficient and water ingress rate could be observed by varying these on both sides of their nominal values. The results of these calculations are shown in Figure 9-9. Similarly, holding the diffusion coefficient constant, allowed for an appreciation of the effect of varying the graphite-water reaction rate. These results are shown on Figure 9-10.

An interesting artifact of these calculations is that, except for roughly the last upper half-decade of the water ingress range, the effect of increasing (or decreasing) the graphite-water reaction rate is the same as increasing (or decreasing) the diffusion coefficient of water in graphite. This result is consistent with the argument that the overall reaction rate should be proportional to not only the graphite-water reaction rate, but also to the ratio of the average steam concentration in the graphite to what it would be if the reaction were truly homogeneous. The first factor is simply the homogeneous reaction rate, R. The second factor is roughly proportional to the diffusion length of steam in graphite* and can be

*This is strictly true only when the diffusion length is smaller than the thickness of graphite reacting with steam (i.e. at the higher temperatures along the coolant channel). However, when this condition is not met, the contribution of the graphite-water reaction to the steady-state impurity concentration is small and therefore can be neglected in comparison to where this condition is met.

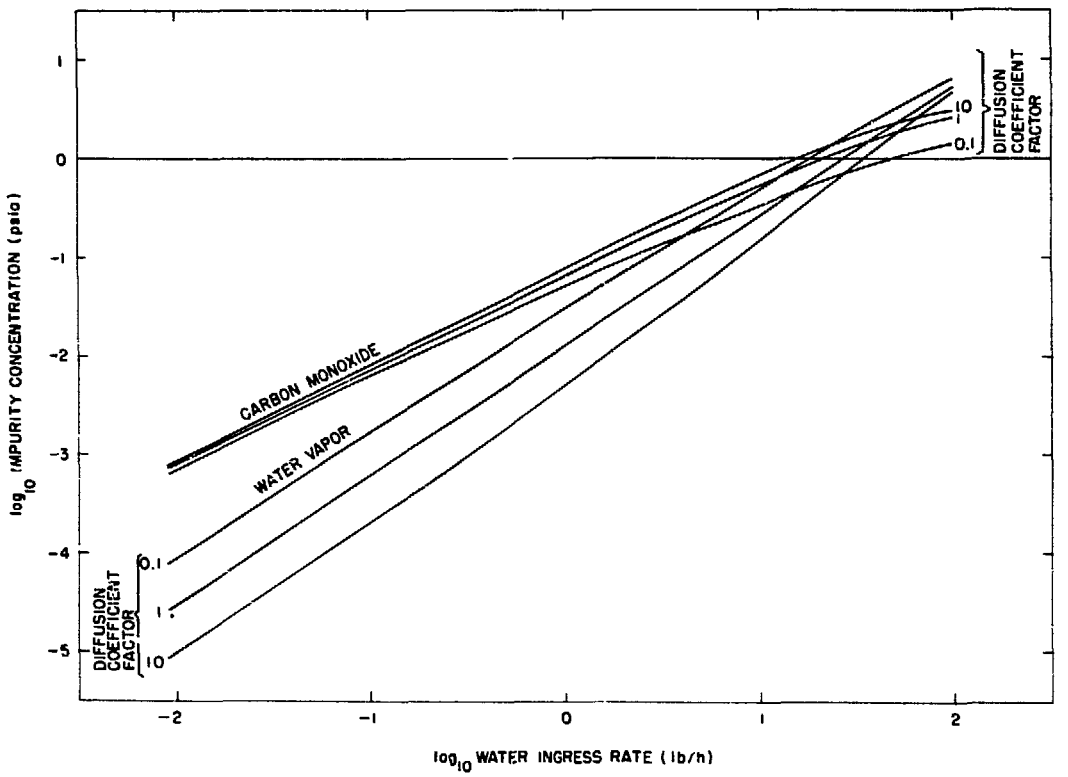

Figure 9-9. Effect of steam-graphite diffusion coefficient.

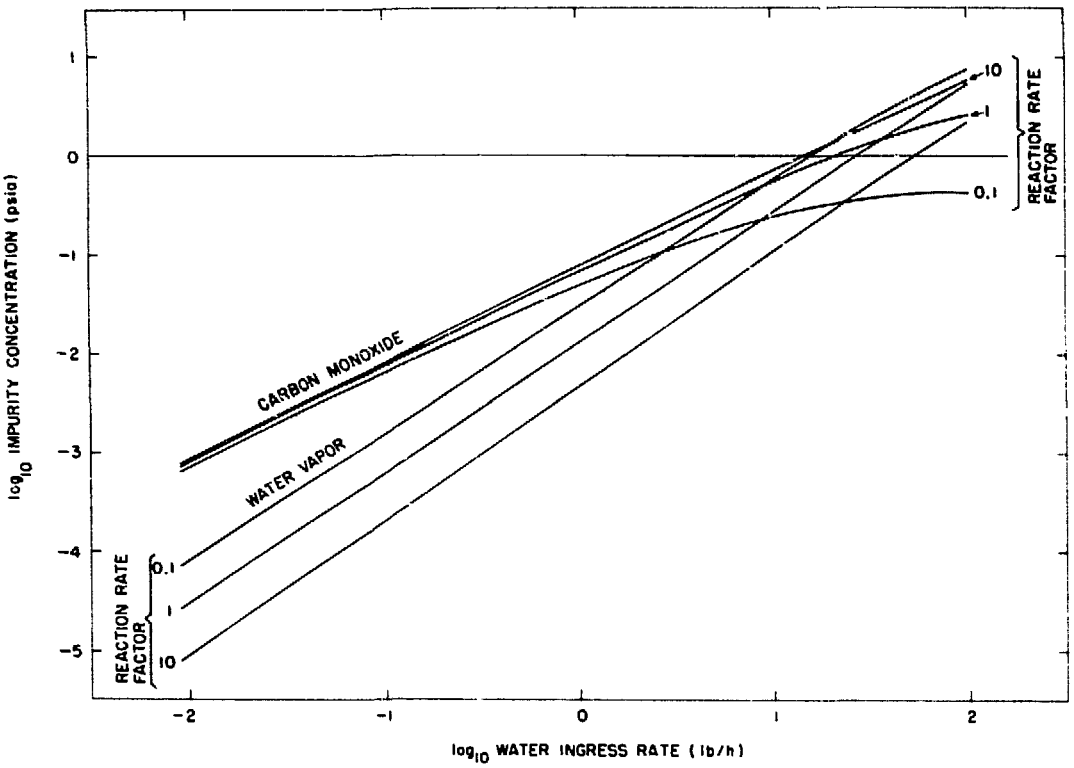

Figure 9-10. Effect of graphite-water reaction rate.

approximated as being proportional to $\sqrt{D/R}$. Therefore, the overall reaction rate should be proportional to $\sqrt{DR}$ and hence, to first order, it is irrelevant whether one increases (or decreases) the reactivity rate or the diffusion coefficient.

D. Group Collapsing of Cross Sections for HTGR's (J. Herczeg)

To correctly generate two-energy "group constants" for a specific reactor, it is necessary to choose:

(1) A computer code and cross section set designed for that specific type of reactor.

(2) An energy group structure representative of the characteristics of the materials within the reactor.

Considered here is the 1160 MW(e) HTGR fueled with ^{232}Th-^{235}U at the beginning-of-life; the approach to group collapsing of cross sections and the recommended specific energy break points are discussed.

Several codes are available which generate broad group "group constants" from their own specific fine mesh cross section libraries. A few of these codes are HAMMER[9-2], GRANIT[9-3], EGGNIT[9-4], MC[9-5], GGC-4[9-5], GGC-5[9-7], and MICROX[9-8]. Of these codes, the most readily available and best suited code for HTGR studies is GGC-4. This code is basically a one-region code with the exception that, for resonance calculations, a fuel stick is considered within the basic cell, creating a pseudo two-region calculation. This approach is acceptable for fuel-moderator calculations; however, it is inadequate for control rods or poison rod regions. For the latter case, the

general approach is to utilize transport theory through one or more basic codes such as ANISN[9-9] and TWOTRAN[9-10]. ANISN is a one-dimensional transport code which accepts group collapsed macroscopic cross sections. GGC-4 can supply these cross sections region-by-region to set up a multi-region ANISN calculation. ANISN can then collapse to a few groups which can supply a two-dimensional code such as TWOTRAN which can collapse "group constants" to two broad energy groups. A flow chart of the approach is shown in Figure 9-11.

The generation of two-group "group constants" requires the appropriate selection of a thermal-fast energy break point which separates the thermal regime from the resonance reactions. This choice is generally made on the recommendation that the cut point be high enough to include most of the up-scattering which occurs in the energy range. A typical energy break point chosen is 2.38 eV[9-11], and shall be used throughout this memo.

The collapsing of fast-group cross sections (2.38 eV → 14.6 MeV) from a one-dimensional code such as GGC-4 should be conducted in a manner which takes into account the properties of the primary materials which make up the reactor. Examples of these primary materials for a typical beginning-of-life HTGR are: ^{232}Th, ^{235}U, and ^{238}U.

The first major consideration is the threshold of ^{232}Th fission which is approximately 1.2 MeV[9-12]. The second consideration is the upper-energy break point of the resolved energy region which is 1.58 keV for ^{232}Th and 3.35 keV for ^{238}U. The last consideration

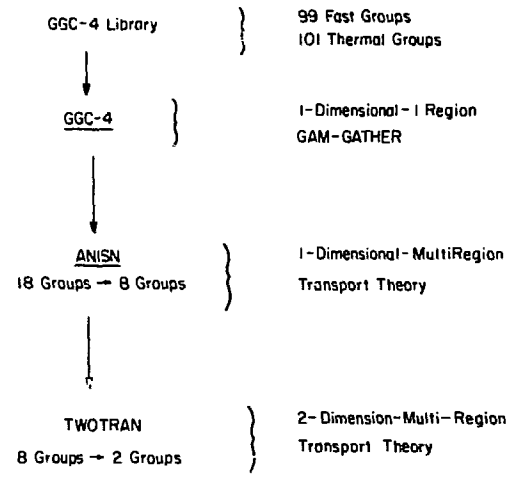

Figure 9-11. Flow diagram of group collapsing approach for HTGR few group "group constants".

is the separation of the 21.78 eV and the 23.45 eV ^{232}Th resonances. Utilizing these considerations, a four-group "fast energy" break point scheme can be generated with approximately equal lethargy widths. Sub-division of these four groups, with careful consideration given to ^{232}Th resonances, gives a nine-group ANISN scheme. Table 9-7 and Figure 9-12 tabulate and describe graphically the recommended nine-group ANISN and four-group TWOTRAN energy break point schemes.

The collapsing of thermal cross sections (0.0 → 2.38 eV) to one set of "group constants" is handled under a different criteria. In the lower energy region, the primary materials have cross sections which behave inversely proportional to the velocity of the neutron ($\sigma_a \alpha 1/v$). One primary absorption material of importance is boron in the form of B_4C. The basis of the group structure for the thermal region could thus be based upon either of the following two conditions:

$$(1) \quad \int_{\Delta E} \sigma_a^B (E)\, \varphi (E) \sim \text{same for each group}$$

$$(2) \quad \int_{\Delta E} \frac{D}{\Sigma_a} (E)\, \varphi (E) \sim \text{same for each group}$$

This discussion considers condition (1). Leakage consideration (condition (2)), however, would be equally valid.

The determination of equal absorption groups (condition (1)) requires a knowledge of the thermal neutron flux spectrum, over which

Table 9-7

Fast Energy Break Points for ^{232}Th-^{235}U Fueled HTGR's

Group Number	ANISN	TWOTRAN	U
	14.9 +06	14.9 +06	0.0
1	2.23+06		1.8994
2	1.35+06		2.4013
3	3.02+05	3.02+05	3.899
4	4.09+04		5.898
5	3.35+03	3.35+03	8.400
6	7.49+02		9.898
7	1.01+02	1.01+02	11.902
8	2.26+01		13.399
9	2.38	2.38	2.38

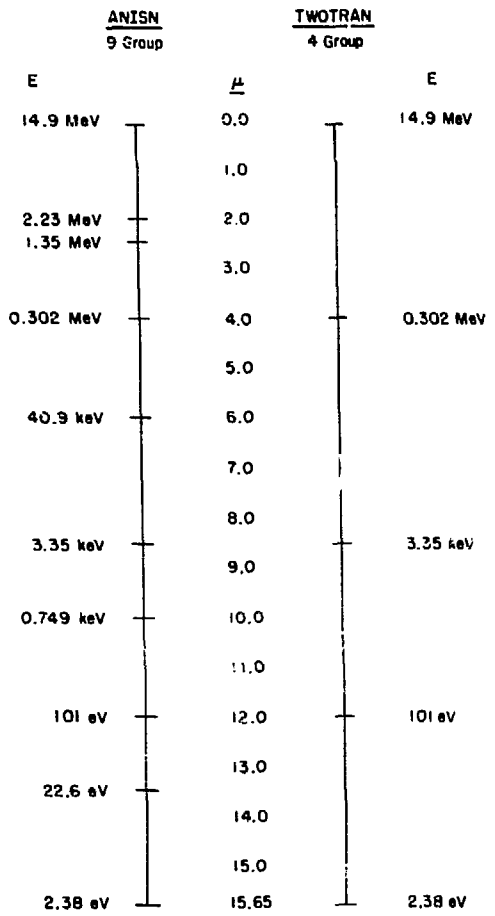

Figure 9-12. Few-group epithermal breakpoints for ANISN and TWOTRAN accommodated to ^{232}Th-^{235}U fueled HTGR's.

the calculation may be conducted. Figure 9-13 describes such a spectrum. The resulting four-group TWOTRAN break points are tabulated in Table 9-8 and graphically described in Figure 9-14.

E. SORS (J. M. Dickey)

The SORS computer program is designed to calculate the maximum hypothetical fission product release following an accident involving the complete loss of the primary coolant or during some other transient temperature excursion. There are two versions of SORS: (1) SORSD which deals with the volatile fission products only and (2) SORSG which also treats the nonvolatile fission products. SORSG is not yet available, but SORSD has now been adapted to the CDC 7600 and replicates, for the volatile fission products, the trial problem supplied by GA. The input data for SORSD are the initial inventory of fission products, which will depend on the prior operating history of the reactor, and the temperature evolution of the reactor following the accident. The natural decay of the fission products provides the heat source and the necessary temperature sequence can be calculated in CORCON, using certain conservative assumptions concerning the migration of the fission products.

In SORSD, coupled differential equations are solved for each decay chain using an average rate at which the individual isotopes can escape from the fuel particles. This average release rate for the whole reactor, depends on time, and is calculated by splitting the core into 56 regions and using the temperature history of each region

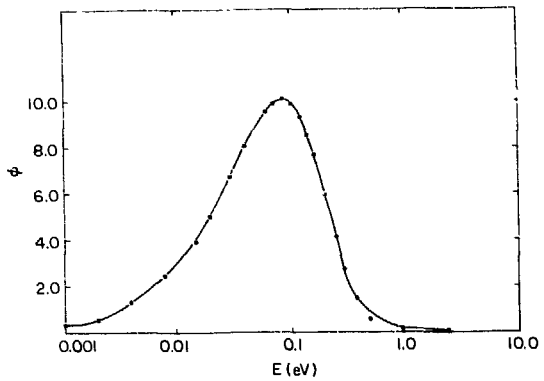

Figure 9-13. Thermal neutron flux spectrum for ^{232}Th-^{235}U (c/u = 1300:1) HTGR at fuel temperature of 1255°K.

Table 9-8

Thermal Energy Break Points for ^{232}Th-^{235}U Fueled HTGR's

Group Number	ANISN	TWOTRAN
	2.38	2.38
1	0.30	
2	0.22	0.22
3	0.16	
4	0.12	0.12
5	0.085	
6	0.060	0.06
7	0.040	
8	0.001	0.001

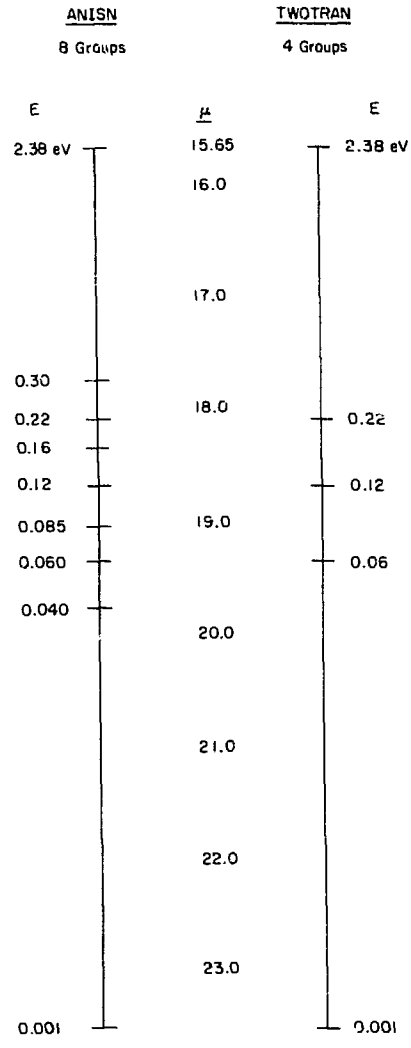

Figure 9-14. Few-group thermal breakpoints for ANISN and TWOTRAN accommodated to ^{232}Th-^{235}U fueled HTGR's.

which has previously been calculated by CORCON. For any particular region the instantaneous release rate can be found from the temperature and the experimental data on escape rates from the fuel particles. In order to find an overall release rate the weighting factor for each region must be estimated. These weighting factors depend on time and are calculated using a simplified differential equation neglecting nuclear decay, or in other words it is assumed the amount of activity remaining in the region decreases only because of escape from the fuel. The internal self consistency of this assumption is being examined.

The coatings of the fuel particles fail in the range 2000-2600^{o}F, and these temperatures are attained after about 2-3 hours by most of the particles. However, the escape rates from fuel particles only become large at high temperatures, so the initial fraction of intact particles does not affect the fission product release for times longer than about 3 hours. If it is assumed that all the particles have failed prior to the start of the accident, the amount released would differ only during the first 2 to 3 hours but during this time, the actual amount released is only about 1% of the total inventory. After 2 hours the amount of ^{131}I released, assuming all the particles had failed at the outset, is 17% larger than if particle failure occurs continuously as the core heats up; but at this time less than 1% of the final amount of ^{131}I has been released. The significant fuel particle parameters controlling

the release of fission products are the escape coefficients at high temperatures, and these are extrapolated from experimental data which have been obtained at lower temperatures. Due to the high temperatures occurring after the accident, it is the escape rates which are important, not the temperature range of failure of the coatings.

References

9-1 HTGR Safety Evaluation Division Quarterly Progress Report, April-June 1975, BNL-50460.

9-2 J. E. Suich and H. C. Honeck, "The HAMMER System - Heterogeneous Analysis by Multi-group Methods of Exponentials and Reactors," DP-1064, Savannah River Laboratory (1964).

9-3 C. L. Bennett, "GRANIT: A Code for Calculating Position Dependent Thermal Neutron Spectra in Doubly Heterogeneous Systems by the Integral Transport Method," Technical Activities Quarterly Report, AEC Reactor Development and Technology Programs, July, August, September, 1970, BNWL-1522-1.

9-4 C. R. Richey, "EGGNIT: A Multigroup Cross Section Code," BNWL-1203, Pacific Northwest Laboratories, Battelle Memorial Institute, Richland, Washington, November 1969.

9-5 B. J. Toppel, A. L. Rago, and D. M. O'Shea, "MC^2, A Code to Calculate Multigroup Cross Sections," Argonne National Laboratory report ANL-7318 (1967).

9-6 J. Adir and K. D. Lathrop, "Theory of Methods Used in the GGC-4 Multigroup Cross Section Code," GA-9021, General Atomic (1968).

9-7 D. R. Mathews, et al.,"GGC-5, A Computer Program for Calculating Neutron Spectra and Group Constants," GA-8871, General Atomic (1971).

9-8 P. Walti and P. Koch, "MICROX, A Two-Region Flux Spectrum Code for the Efficient Calculation of Group Constants," GA-A10827, Gulf General Atomic (1972).

9-9 W. W. Engle, Jr., "The User's Manual for ANISN: A One-Dimensional Discrete Ordinates Transport Code with Anisotropic Scattering," Union Carbide Corp. report K-1693 (1967).

9-10 K. D. Lathrop and F. W. Brinkley, "TWOTRAN-II: An Interfaced, Exportable Version of the TWOTRAN Code for Two-Dimensional Transport," Los Alamos Scientific Laboratory, LA-4848-MS (1973).

9-11 R. G. Bardes, et al., "Results of HTGR Crtical Experiments Designed to Make Integral Checks on the Cross Sections in Use at Gulf General Atomic," GA-8468, Gulf General Atomic (1968).

9-12 D. E. Cullen and P. J. Hlavac, "ENDF/B Cross Sections," BNL-17100 (ENDF-200) (1972).

X. Review of Group Activities

A. Review of the Maximum Hypothetical Fission Product Release (MHFPR) and a Proposed Loop Experiment (D. Chandra, H. Isaacs)

The MHFPR is defined in GASSAR[10-1] in terms of the initial conditions at the onset of the MHFPR event and the assumptions governing the state of the plant and the transport processes. The initial conditions establishing the onset of unrestricted core heat up are: (1) the fuel, moderator, reflector and primary system component temperatures correspond to the conditions in the HTGR immediately following reactor trip from 105% power, (2) the inventory of fission products corresponds to the "end-of-cycle shutdown of the equilibrium core operating at full rated power at an 80% plant load factor." The four segments of the fuel loading are 1, 2, 3, and 4 years old. The inventory of fission products, therefore, should correspond to a heavily irradiated core in any experimental simulation attempt to obtain maximum release results, (3) the core after-heat rate is based on 4-year operation of the entire core (at 105% power and an 80% load factor), (4) the primary system pressure is in equilibrium with the containment pressure, and (5) the design primary coolant inventory of radionuclides (Table 11.1-5 in GASSAR) along with certain fractions of fission product plateout activity are assumed to be released to the containment atmosphere at time zero. These fractions are: iodine, 1.1%; strontium, 0.7%; cesium, 0.06%; all other solids, 1.1%.

The experimental data background of these liftoff values (apparently during depressurization) have not been identified. Therefore, the possibility of increased liftoff during depressurization remains open. Furthermore, no consideration has been given to any possible effect of depressurization on the remaining fission product distribution and deposition in the reactor. A better definition of these initial conditions needs to be obtained for a truly appropriate study of fission product release due to core heat up.

Following the description of the "initial conditions" a set of "defining assumptions" has been mentioned in GASSAR. It is important to carefully review the values of various physical and chemical properties mentioned in this section.

The possibility of a loop experiment to simulate this MHFPR event has been evaluated. The main requirements of an actual loop experiment are outlined very briefly below.

To maximize fission product release and to satisfy the condition of "end-of-cycle shutdown of the equilibrium core" (as given in GASSAR), it is necessary to ensure a large fission product inventory in any test fuel element. This can be simulated by using a highly preirradiated fuel element - fuel rod assembly. To create realistic initial conditions before the actual core heat up begins, particularly with respect to fission product distribution and plateout, it is necessary to simulate a reasonably realistic depressurization accident. In this case, a Pegase or similar loop

has some advantages over an out-of-pile experiment. Data obtained from the CPL 2/4 test currently in progress in France may be of some help in this regard.

Following depressurization, the temperature of the test section may be either increased progressively, as would actually occur during the MHFPR accident defined in GASSAR, or stepwise. For a definitive set of conditions, the loop reaches "steady state" conditions after several hours. Therefore, it is proposed that the temperatures be increased stepwise so that it becomes possible to study fuel failure at each temperature level. The temperature range to be studied should be between 1400°C and 2100°C (with the greatest emphasis placed on the 1600-2000°C range). This is the range where according to the GA data (LTR-15), failure of all of the fuel particle coatings occurs.

During each temperature run, the coolant flow rate will be such as to exceed the maximum gas velocity possible due to convective flow in the core coolant channels during the accident. The flow will be piped directly out of the loop to maximize fission product transport. The fuel burnup and the irradiation damage are intimately related to fuel particle failure. This, in addition to the requirement of a large fission product inventory, as described earlier, makes it essential to use a fuel element irradiated to full exposure.

Since an in-pile test is expensive, it is important to

perform a set of experiments to properly establish the conditions of an in-pile test. Most of these initial tests could be performed out-of-pile. Some advantages of initial out-of-pile experiments are:

1. The temperature profile expected following a reactor trip accompanied by depressurization is considerably less steep than expected to be obtained during normal operation. Therefore, a relatively small diameter test section heated out-of-pile by an external source of heat will not experience conditions greatly different from the actual condition.

2. It is easier to conduct an out-of-pile experiment.

3. It may be possible to go to higher temperatures, since the material of the Pegase loop is no longer a limiting factor.

Reference

10-1 General Atomic Standard Safety Analysis Report (GASSAR), GA-A-13200, Chapter 2, General Atomic Company, San Diego, California.